Studies on Fluid–Thermal–Structural Coupling for Aerothermoelasticity in Hypersonic Flow

Adam J. Culler* and Jack J. McNamara†
Ohio State University, Columbus, Ohio 43210

The field of aerothermoelasticity plays an important role in the analysis and optimization of airbreathing hypersonic vehicles, impacting the design of the aerodynamic, structural, control, and propulsion systems at both the component and multidisciplinary levels. This study aims to expand the fundamental understanding of hypersonic aerothermoelasticity by performing systematic investigations into fluid–thermal–structural coupling. A focus is on the targeted use of simplified coupling procedures in order to abate the computational effort associated with comprehensive aerothermoelastic analysis. Because of the fundamental nature of this work, the analysis is limited to cylindrical bending of a simply supported, von Kármán panel. Multiple important effects are included in the analysis: namely, 1) mutual coupling between elastic deformation and aerodynamic heating, 2) transient arbitrary in-plane and through-thickness temperature distributions, and 3) the associated thermal stresses and material property degradations. It is found that including elastic deformations in the aerodynamic heating computations results in nonuniform heat flux, which produces nonuniform temperature distributions and material property degradations. This results in localized regions in which material temperature limits may be exceeded; it also impacts flutter boundary predictions and nonlinear flutter response. Additionally, the tradeoff between computational cost and accuracy is evaluated for aerothermoelastic analysis based on either quasi-static or time-averaged dynamic coupling. It is determined that these approaches offer substantial reductions in computational expense, with negligible loss of accuracy, for aerothermoelastic analysis over long-duration hypersonic trajectories.

Nomenclature

A_m, A_n	=	amplitude of mth and nth sine modes, respectively
a	=	panel length, chordwise
C_i	=	ith coefficient in polynomial mode
c	=	specific heat
c_f	=	local skin-friction coefficient
c_p	=	specific heat at constant pressure, air
D	=	bending stiffness of panel
D_{dome}	=	diameter of spherical dome protuberance
E	=	elastic modulus
F_m	=	terms dependent on modal amplitudes and velocities
H	=	enthalpy
H_{PD}	=	height of spherical pressure-instrumented dome
H_{TD}	=	height of spherical thermocouple-instrumented, heat-flux dome
h	=	thickness of plate structure
h_c	=	convection heat transfer coefficient
h_i	=	thickness of ith panel layer
k	=	thermal conductivity
M	=	Mach number
M_T	=	thermal bending moment
N	=	number of sine modes
N_T	=	in-plane thermal force
N_x	=	in-plane stress resultant
Pr	=	Prandtl number
p	=	pressure
Q	=	heat flux
Q_{aero}	=	aerodynamic heat flux
Q_{conv}	=	convection heat flux
Q_{rad}	=	radiation heat flux
q	=	$\rho U^2/2$, dynamic pressure
q_a	=	$p - p_3$, aerodynamic pressure on panel surface
R_{eq}	=	equivalence ratio, equals fuel-to-air ratio divided by stoichiometric fuel-to-air ratio
Re_x	=	local Reynolds number
r	=	recovery factor
St	=	Stanton number
T	=	temperature
T_{env}	=	environment temperature
T_{initial}	=	initial uniform panel temperature
T_{ref}	=	stress-free reference temperature
t	=	time
U	=	velocity, air
u	=	panel displacement, chordwise
u_0	=	midplate displacement, chordwise
w	=	panel displacement, transverse
w_0	=	midplate displacement, transverse
x	=	chordwise direction, parallel to flat panel surface
x_3	=	distance from transition to turbulence to leading edge of panel
Y_m	=	velocity of mth sine mode
z	=	transverse direction, normal to flat panel surface
α	=	thermal expansion coefficient
β	=	oblique shock angle relative to freestream
Γ	=	parameter in nondimensional temperature
γ	=	ratio of specific heats, air
Δ	=	incremental change
δ_x	=	mean relative edge displacement
ϵ	=	emissivity
η	=	viscosity, air
θ	=	rigid surface (panel-holder) inclination angle to freestream
λ	=	nondimensional dynamic pressure
μ	=	air/plate mass ratio
ν	=	Poisson's ratio
ρ	=	density
ρ_i	=	density of ith panel layer
ρ_p	=	density of plate structure

*Ph.D. Candidate, Department of Aerospace Engineering. Student Member AIAA.

†Assistant Professor, Department of Aerospace Engineering. Senior Member AIAA.

σ	=	Stefan-Boltzmann constant, 5.669×10^{-8} W/m^2/K^4
σ_x	=	normal stress
σ_0	=	parameter in nondimensional stress
τ	=	parameter in nondimensional time
ϕ	=	nondimensional equation of motion

Subscripts

AE	=	aeroelastic
AT	=	aerothermal
aw	=	adiabatic wall
cr	=	critical value
e	=	edge of boundary layer
fp	=	flat plate
i, j	=	node indices in x direction and z direction
L, U	=	lower and upper surfaces of plate structure
m, n	=	sine mode numbers
PD	=	pressure-instrumented dome
TD	=	thermocouple-instrumented, heat-flux dome
w	=	wall, aerodynamic surface
x, z	=	x direction, z direction
0	=	total condition (flow variable) or reference value (material property)
3	=	flow at leading edge of panel
∞	=	freestream

Superscripts

n	=	time-step index
$^-$	=	nondimensional
$*$	=	evaluated at the reference enthalpy

I. Introduction

CURRENTLY, there is a focus by NASA and the U.S. Department of Defense on the development of hypersonic technologies for next-generation reusable launch vehicles and unmanned hypersonic cruise vehicles [1–6]. Modern hypersonic cruise vehicle configurations are typically based on a lifting-body, integrated airframe-propulsion concept, in which the entire lower vehicle surface is part of a scramjet engine. An example of this concept is the NASA X-43 aircraft shown in Fig. 1. These vehicles will operate over a Mach number range of 0 to 15 and must fly within the atmosphere for sustained periods of time to meet the needs of the propulsion system [2–5,7–12]. This latter constraint results in severe aerodynamic heating of the vehicle, which significantly alters the structure through material property degradations and the development of thermal stresses. Collectively, these issues result in a tight coupling between the aerodynamic, control, structural, and propulsion systems that cannot be neglected in the analysis and design of this class of vehicle [5–7,13–16]. Furthermore, due to the
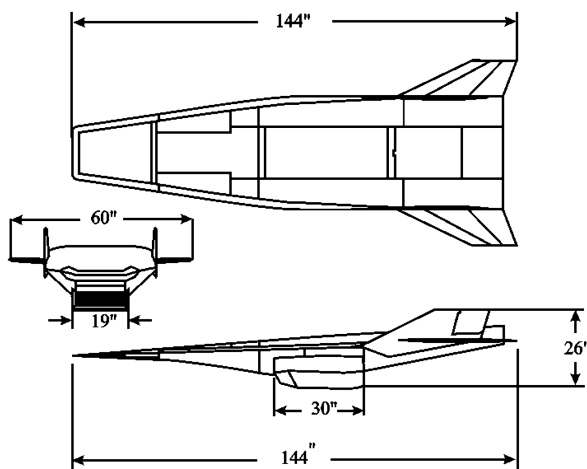
impracticality of testing scaled multidisciplinary models in wind tunnels [17], the development of tractable and accurate computational modeling capabilities is critical for this flight regime [18].

The presence of extreme aerodynamic pressure and heating in hypersonic flow, combined with the need for optimal weight structures, implies that the field of aerothermoelasticity plays a central role in the analysis and optimization of hypersonic vehicles and components [18]. A recent review paper [18], in addition to several early studies [19–28], provides insight into the salient aspects of aerothermoelasticity. Consider Fig. 2, which illustrates the degree of coupling between the different disciplines that compose the field [23]. Typically, the aerothermoelastic problem is simplified by neglecting weak couplings, as well as the effect of aerodynamic pressure on aerodynamic heating. In such an approach, the aerothermal solution is obtained first, using a reference geometry of the vehicle, over the entire range of relevant operating conditions. Subsequently, the aeroelastic analysis is carried out using an updated structure based on the resulting temperature distribution. This simplification of the aerothermoelastic problem is denoted here as *one-way coupling*, and relies on three important assumptions [19,23,24,26]:

1) Thermodynamic coupling between heat generation and elastic deformation is negligible.

2) Dynamic aeroelastic coupling is small; i.e., the characteristic time of the aerothermal system is large relative to the time periods of the natural modes of the aeroelastic system.

3) Static aeroelastic coupling (static elastic deflections due to steady-state pressure and thermal loading) is insufficient to alter the temperature distribution from the reference condition.

Under conditions where these assumptions fail, feedback from the aeroelastic solution to the aerothermal solution is required in order to update the aerodynamic heating conditions based on structural deformation. This procedure is denoted here as *two-way coupling*. Part of the focus of this paper is to investigate the above two procedures for aerothermoelasticity in hypersonic flow.

Relevant studies conducted in hypersonic aerothermoelasticity can be divided into two main groups: 1) panel flutter, which is a localized aeroelastic problem of skin panels, and 2) control surface and vehicle level studies [18]. Numerous studies have investigated thermal effects on panel flutter at hypersonic speeds [29]; however, with few exceptions [30–32], temperature distributions in the panel were simply prescribed. The temperature distributions considered can be separated into three types: namely, 1) uniform, 2) nonuniform in-plane, with uniform through-thickness, and 3) nonuniform through-thickness, with either uniform or nonuniform in-plane. Temperature distribution types 1 and 2 yield in-plane thermal forces only, whereas type 3 produces in-plane thermal forces and thermal bending moments.

Numerous panel flutter investigations have examined the effects of type 1 [25,30,33–42], and type 2 [31,32,43–46], temperature distributions; however, only a limited number of studies have

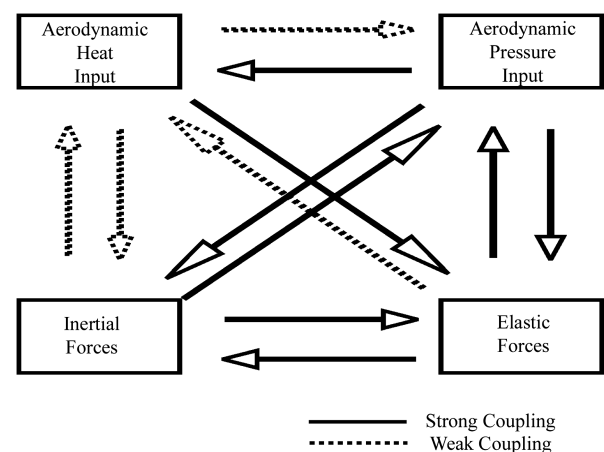Fig. 1 NASA X-43 airbreathing hypersonic vehicle.

Fig. 2 Degree of coupling in aerothermoelasticity [23].

investigated type 3 temperature distributions [47–52]. Xue and Mei [47] considered linear through-thickness gradients combined with sinusoidal in-plane temperature distributions in a three-dimensional isotropic panel using a nonlinear finite element, frequency-domain method. Nydick et al. [48] extended the analytical model used in [37] to include linear, sinusoidal, and quadratic in-plane temperature distributions combined with linear through-thickness gradients in a curved orthotropic panel. Cheng et al. [49] and Cheng and Mei [50] investigated thermal effects on isotropic and laminated composite plates by considering an average uniform temperature combined with a linear through-thickness gradient. Nonlinear finite element models were used in both studies; a frequency-domain method was employed in [49], and a time domain modal formulation was developed in [50]. Recently, Ghoman et al. [52] extended the methods used in [49] to investigate uniform in-plane temperature combined with a linear through-thickness gradient in curved isotropic and laminated composite panels.

It is interesting that even though material property degradation is dependent on the temperature distribution, few panel flutter investigations have examined the combined effect [42,46,51]. Librescu et al. [46] studied the effects of temperature-dependent elastic modulus and thermal expansion coefficient for sinusoidal in-plane (uniform through-thickness) temperature distributions in a semi-infinite isotropic panel. Prakash and Ganapathi [51] investigated the effects of linear through-thickness (uniform in-plane) temperature gradients in a three-dimensional functionally graded material panel. Functionally graded material panels were also recently investigated by Ibrahim et al. [42] for thermal buckling and nonlinear flutter under uniform temperature.

Despite its potential importance, only limited work has considered two-way coupling. Two-way coupling was approximated in two panel flutter studies [31,32], by assuming that the panel temperature is equal to the steady-state adiabatic wall temperature plus the instantaneous local fluid temperature. The instantaneous local fluid temperature as a function of deformation was computed using an isentropic pressure–temperature relationship, where the deformation-dependent pressure was computed from linear piston theory [29,53]. In related work, two-way coupling was considered for aerodynamically heated panels [54] and leading edges [55] using a quasi-static loosely coupled finite element approach for the flow, thermal, and structural models. Two-way quasi-static coupling was also considered for metallic thermal protection panels [56] using a two-dimensional boundary element procedure that was loosely coupled to a hypersonic computational fluid dynamics algorithm. Results of these studies demonstrated a significant dependence of the aerodynamic heating on structural deformation. However, since these studies were limited in scope and/or modeling, more work is needed to fully understand the importance of two-way coupling for modeling the aerothermoelastic behavior of hypersonic structures.

Because of the increased complexity of the problem, studies in the second group (i.e., hypersonic aerothermoelastic analysis of wings and complete vehicles), are limited [18]. Recent investigations have focused on modern vehicle concepts such as the National Aerospace Plane (NASP) [57–59] and the Force Application and Launch from Continental United States (FALCON) vehicles [60]. However, these studies only considered one-way coupling. In [57–59] the temperature distribution was prescribed based on steady-state aerodynamic heating analysis. Alternatively, McNamara et al. [60] considered transient heat transfer analysis, where the aerodynamic heating boundary condition was computed from a Navier–Stokes flow analysis of a rigid control surface along a representative trajectory. Note that only [59,60] considered the effects of both material property degradation and thermal stresses.

This study is motivated by the need for an improved general understanding of fluid–thermal–structural coupling for aerothermoelastic analysis in hypersonic flow. The aim is to explore several fundamental aspects of the aerothermoelastic problem, at the fluid–structure interchange, that have not yet received adequate attention. Because of its fundamental nature, this study uses a simply supported, semi-infinite panel as the structural model. The specific objectives of the paper are as follows:

1) Develop a computationally efficient, comprehensive, two-way coupled aerothermoelastic model in order to study the importance of fluid–thermal–structural coupling in hypersonic flow.

2) Investigate quasi-static and time-averaged dynamic fluid–thermal–structural coupling procedures in order to reduce the computational expense of comprehensive aerothermoelastic analysis.

3) Assess the sensitivity of aerothermoelastic response in hypersonic flow to different types of fluid–thermal–structural coupling.

Fulfilling these objectives will make a valuable contribution towards our understanding of hypersonic aerothermoelasticity and towards the development of comprehensive computational models of airbreathing hypersonic vehicles. Specifically, new insight is gained in the following areas: 1) methodology to include transient thermal effects and two-way coupling in the computation of aerothermoelastic response along an entire trajectory; 2) the impact on the flutter boundary and postflutter response of neglecting two-way coupling; and 3) the impact of using simplified temporal coupling procedures (i.e., quasi-static and time-averaged dynamic) to predict aerothermoelastic behavior.

II. Aerothermoelastic Model Formulation

The aerothermoelastic model developed in this investigation is illustrated in Fig. 3. The general problem is divided into aerothermal and aeroelastic components, with two-way coupling included. The structural temperature distribution is passed from the aerothermal model to the aeroelastic model along path 1. Feedback of elastic deformation to the aerothermal model is transferred along path 2. Note that thermodynamic coupling between heat generation and elastic deformation is neglected during the two-way coupling process.

A. Aerodynamic Pressure

Because of the comprehensive nature of the present work, a computationally efficient unsteady aerodynamic theory is essential for model tractability. Therefore, piston theory [29,53], which provides a simple point-function relationship between the unsteady pressure and surface motion, is selected for computing the unsteady aerodynamic loads on the panel. While piston theory represents a simplistic model for the inviscid aerodynamics, it has been observed in several studies [18] to provide reasonably accurate pressure predictions as long as the product of Mach number and surface inclination remains below unity.

The panel considered in this study is located on an inclined surface of a wedge-shaped body, representing the forebody of a hypersonic cruise vehicle, as shown in Fig. 4. The freestream flow (location 1) is hypersonic, resulting in an attached oblique shock at the forebody leading edge [13]. The inclined surface before and after the panel is assumed to be flat and rigid; thus, the inviscid flow properties at the leading edge of the panel (location 3) are the same as location 2. Therefore, the third-order piston theory expression given by Eq. (1) uses the local flow properties at location 3 as the ambient panel
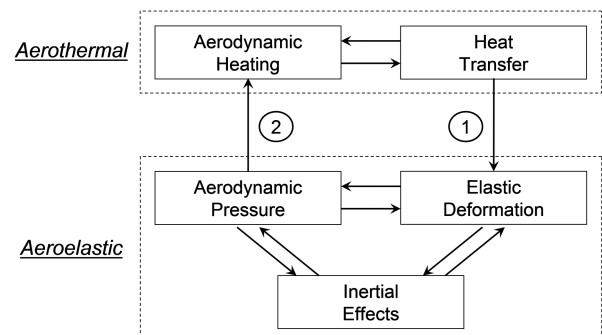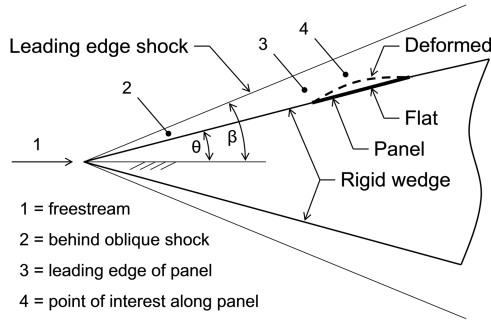

Fig. 3 Aerothermoelastic model based on two-way coupling of aerothermal and aeroelastic components.

Fig. 4 Panel located on an inclined surface of a wedge-shaped forebody.

conditions. These properties are computed using oblique shock relations [61,62], and the undeformed configuration of the panel is parallel to this flow. Note that a third-order expansion of piston theory is used in this study, due to the combined presence of hypersonic flow conditions and large panel deflections [29,63]:

$$q_a = 2\frac{q_3}{M_3}\left[\left(\frac{1}{U_3}\frac{\partial w}{\partial t} + \frac{\partial w}{\partial x}\right) + \frac{\gamma+1}{4}M_3\left(\frac{1}{U_3}\frac{\partial w}{\partial t} + \frac{\partial w}{\partial x}\right)^2 \right.$$
$$\left. + \frac{\gamma+1}{12}M_3^2\left(\frac{1}{U_3}\frac{\partial w}{\partial t} + \frac{\partial w}{\partial x}\right)^3\right] \tag{1}$$

B. Aerodynamic Heating

Aerodynamic heating from the boundary layer is computed using Eckert's reference enthalpy method [64]. This semi-empirical method uses boundary-layer relations from incompressible flow theory with flow properties evaluated at a reference condition to account for the effects of compressibility. Reference enthalpy methods have been used extensively in approximate analyses to efficiently model convective heating of aerospace vehicles [65–70].

Eckert's reference enthalpy is given by Eq. (2). The adiabatic wall enthalpy, the total enthalpy, and the recovery factor for turbulent flow are given in Eqs. (3–5), respectively [64]. Note that local velocity and enthalpy at the edge of the boundary layer are determined from the local edge Mach number and temperature, respectively. Mach number and temperature at the edge of the boundary layer are computed using the local pressure from piston theory, Eq. (1), in conjunction with isentropic flow relations [61]. Thus, aerodynamic heating computations include flow effects due to the deformed panel shape and the normal panel velocity (i.e., feedback of elastic deformation to the aerothermal model, path 2 in Fig. 3). For one-way coupling, the boundary-layer edge properties are based on flow over the undeformed (flat) panel throughout the aerothermoelastic analysis:

$$H^* = H_e + 0.50(H_w - H_e) + 0.22(H_{aw} - H_e) \tag{2}$$

$$H_{aw} = r(H_0 - H_e) + H_e \tag{3}$$

$$H_0 = H_e + \frac{U_e^2}{2} \tag{4}$$

$$r = (Pr^*)^{1/3} \tag{5}$$

Using flow properties evaluated at the reference enthalpy, the aerodynamic heat flux is computed using Eq. (6). The Stanton number is determined from the Colburn–Reynolds analogy [64,71] provided in Eq. (7), and the local skin-friction coefficient is calculated using the Schultz–Grunow formula [64,71] given in Eq. (8). The local Reynolds number is defined in Eq. (9) and is computed using the distance from the onset of transition to the point

of interest along the panel [71]. In this investigation, the leading edge of the panel is assumed to be 1 m downstream of the onset of transition. The complete transition from laminar to turbulent flow is assumed to occur within this region, such that flow over the panel is fully turbulent:

$$Q_{aero} = St^* \rho^* U_e (H_{aw} - H_w) \tag{6}$$

$$St^* = \frac{c_f^*}{2}\frac{1}{(Pr^*)^{2/3}} \tag{7}$$

$$c_f^* = \frac{0.370}{(\log_{10} Re_x^*)^{2.584}} \tag{8}$$

$$Re_x^* = \frac{\rho^* U_e x}{\eta^*} \tag{9}$$

In addition to Eqs. (2–9), temperature-enthalpy relations are needed to determine the values of enthalpy at the wall and at the edge of the boundary layer. These relations are also required to determine a temperature from the reference enthalpy in order to evaluate reference density and reference viscosity using the ideal gas law and Sutherland's law, respectively [13]. If the flow is assumed to be calorically perfect, i.e., constant specific heat, then Eq. (10) is used and the reference enthalpy method is equivalent to the reference temperature method [64]. However, since this study is concerned with hypersonic flow, in which the specific heat varies significantly through the boundary layer, due to high temperatures and real gas effects [13], temperature-enthalpy tables [72] that include the effect of dissociation based on equilibrium air properties are employed:

$$H = c_p T \tag{10}$$

C. Aerothermal Model

The aerothermal model, illustrated in Fig. 5, accounts for aerodynamic heating and thermal radiation at the surface, as well as transient heat transfer through the multilayer thermal structure. The thermal structure considered in this study consists of a thermal protection system (TPS) and a titanium plate structure. The TPS is based on the Advanced Metallic Honeycomb TPS concept [73]. The radiation shield is a PM-2000 honeycomb sandwich and the thermal insulation is internal multiscreen insulation. A high-temperature grade of titanium (Ti-6Al-2Sn-4Zr-2Mo) is used for the plate structure [74,75]. The thermophysical properties and thickness of each layer are listed in Table 1. Note that specific heat and thermal conductivity are temperature-dependent. Data for these properties as a function of temperature are provided by [73] for the radiation shield and the thermal insulation, and by [75] for the plate structure.
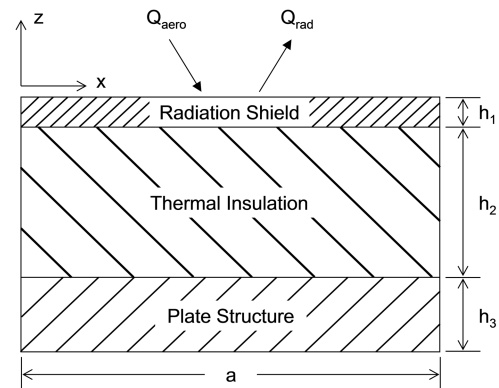
Fig. 5   Two-dimensional model of the thermal structure.

Table 1 Properties of the thermal structure at 300 K

	ρ, kg/m³	c, J/kg/K	k, W/m/K	h_i, mm
Radiation shield	1010	465	0.250	2.0
Thermal insulation	73.0	729	0.0258	10.0
Plate structure	4540	463	6.89	5.0

Transient heat transfer in the panel is modeled using the two-dimensional heat equation [76], Eq. (11), for chordwise and through-thickness directions. The three layers of the panel are assumed to be in perfect thermal contact; i.e., no gaps exist between layers and thermal contact resistance is negligible. The boundary condition along the upper surface includes aerodynamic heating from Eq. (6), and thermal radiation given by Eq. (12). Thermal radiation is modeled by considering the upper surface to be nonblack, diffuse, and enclosed by the environment [77]. The environment temperature is assumed to be constant at 300 K. Emissivity of the radiation shield [73] is assumed to have a constant value of 0.7. An adiabatic boundary condition is applied to the lower surface and edges of the panel:

$$\rho c \frac{\partial T}{\partial t} = k_x \frac{\partial^2 T}{\partial x^2} + k_z \frac{\partial^2 T}{\partial z^2} \qquad (11)$$

$$Q_{\text{rad}} = \sigma \epsilon (T_w^4 - T_{\text{env}}^4) \qquad (12)$$

D. Aeroelastic Model

The aeroelastic model is illustrated in Fig. 6. The panel is supported by immovable, simple supports, and only transverse oscillations are considered. The equation of motion for a semi-infinite panel undergoing cylindrical bending is developed using von Kármán plate theory [78–80]. Thus, the stress is given by Eq. (13) from Hooke's law for an isotropic homogeneous material (the titanium plate structure) [80]. The assumed displacement field is provided in Eq. (14) [78–80]. Using Eqs. (13) and (14), the equation of motion is given by Eq. (15) in conjunction with Eqs. (1) and (16–19). Three important effects are included in the equation of motion: 1) thermal loading due to arbitrary, in-plane, and through-thickness temperature distributions; 2) chordwise variation of the elastic modulus and the thermal expansion coefficient; and 3) TPS mass (TPS stiffness is neglected):

$$\sigma_x(x,z) = \frac{E(x)}{1-\nu^2}\left[\frac{\partial u}{\partial x} + \frac{1}{2}\left(\frac{\partial w}{\partial x}\right)^2\right] - \frac{E(x)\alpha(x)}{1-\nu}[T(x,z)-T_{\text{ref}}] \quad (13)$$

$$u(x,z) = u_0(x) - z\frac{\partial w}{\partial x}; \qquad w(x,z) = w_0(x) \qquad (14)$$

$$\frac{\partial^2}{\partial x^2}\left(D\frac{\partial^2 w}{\partial x^2}\right) - N_x\frac{\partial^2 w}{\partial x^2} + \left(\sum_i h_i \rho_i\right)\frac{\partial^2 w}{\partial t^2} + q_a + \frac{\partial^2 M_T}{\partial x^2} = 0 \quad (15)$$

$$D = \frac{E(x)h^3}{12(1-\nu^2)} \qquad (16)$$
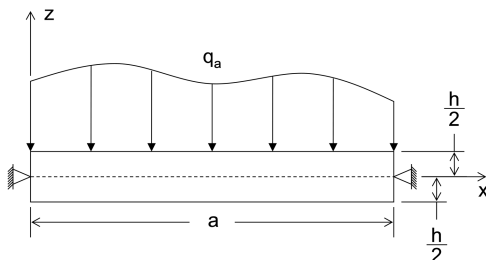
Fig. 6 Simply supported, semi-infinite panel structure.

$$N_x = \int_{-h/2}^{h/2}\sigma_x\, \text{d}z = \frac{E(x)h}{1-\nu^2}\left[\frac{\partial u_0}{\partial x} + \frac{1}{2}\left(\frac{\partial w}{\partial x}\right)^2\right] - N_T \qquad (17)$$

$$N_T = \frac{E(x)\alpha(x)}{1-\nu}\int_{-h/2}^{h/2}[T(x,z)-T_{\text{ref}}]\,\text{d}z \qquad (18)$$

$$M_T = \frac{E(x)\alpha(x)}{1-\nu}\int_{-h/2}^{h/2}[T(x,z)-T_{\text{ref}}]z\,\text{d}z \qquad (19)$$

The stress is rewritten in Eq. (20) using Eqs. (14) and (17), such that each term on the right-hand side corresponds to a unique contribution to the stress field [80]. The first term is a membrane stress caused by in-plane stretching and is uniform through the thickness. The second term is the transverse bending stress, which varies linearly through the thickness. The final term is a thermal stress that is proportional to the temperature distribution:

$$\sigma_x(x,z) = \frac{N_x + N_T}{h} - \frac{E(x)}{1-\nu^2}\left[z\frac{\partial^2 w}{\partial x^2}\right] - \frac{E(x)\alpha(x)}{1-\nu}[T(x,z)-T_{\text{ref}}] \quad (20)$$

To define all variables in Eq. (15) in terms of the transverse displacement and the temperature distribution, the in-plane displacement term $\partial u_0/\partial x$ is eliminated from the expression for N_x in Eq. (17). This is accomplished by introducing the mean relative displacement of the edges of the panel in Eq. (21) (zero for immovable supports) [78]. The final expression for N_x, given in Eq. (22), is developed by solving Eq. (17) for $\partial u_0/\partial x$, substituting the result into Eq. (21), and solving for N_x. In the derivation of Eq. (22), it is important to note that N_x takes on the meaning of an average load in order to approximately satisfy the in-plane boundary conditions [78]. Similarly, the in-plane thermal force, redefined in Eq. (23), also takes on the meaning of an average load. To be consistent with the definitions of N_x and N_T, the third term on the right-hand side of the stress, Eq. (20), is redefined in Eq. (24):

$$\delta_x = -\frac{1}{a}\int_0^a \frac{\partial u_0}{\partial x}\,\text{d}x = 0 \qquad (21)$$

$$N_x = \left[\int_0^a \frac{1}{E(x)}\,\text{d}x\right]^{-1}\int_0^a \frac{h}{2(1-\nu^2)}\left(\frac{\partial w}{\partial x}\right)^2\,\text{d}x - N_T \qquad (22)$$

$$N_T = \left[\int_0^a \frac{1}{E(x)}\,\text{d}x\right]^{-1}\int_0^a \frac{\alpha(x)}{1-\nu}\int_{-h/2}^{h/2}[T(x,z)-T_{\text{ref}}]\,\text{d}z\,\text{d}x \quad (23)$$

$$\sigma_x(x,z) = \frac{N_x + N_T}{h} - \frac{E(x)}{1-\nu^2}\left[z\frac{\partial^2 w}{\partial x^2}\right]$$
$$- \frac{1}{a}\int_0^a \frac{E(x)\alpha(x)}{1-\nu}[T(x,z)-T_{\text{ref}}]\,\text{d}x \qquad (24)$$

The four boundary conditions needed to solve the equation of motion are given in Eq. (25) for $x = 0$, a. The geometric boundary conditions for the simply supported panel are homogeneous; however, the natural boundary conditions are nonhomogeneous, due to the thermal moment [80]:

$$w(x,t) = 0; \qquad \frac{\partial^2 w(x,t)}{\partial x^2} = -\frac{M_T(x,t)}{D(x,t)} \qquad (25)$$

Finally, note that extension of the aerothermoelastic model to a three-dimensional panel is relatively straightforward. The thermal

model can be extended by using the three-dimensional heat equation, and the structural model by incorporating the equations of motion, including thermal stresses, for a two-dimensional plate. The aerodynamic models (piston theory and Eckert's reference enthalpy method) can be applied in a strip sense; however, crossflow effects are not captured.

III.   Method of Solution

As illustrated in Fig. 7, the aerothermoelastic problem is solved using a partitioned approach [81] to couple the aerothermal and aeroelastic solutions. A partitioned approach is advantageous for this problem, since it enables the use of relatively independent solution procedures, as well as different size time steps, for the aerothermal and aeroelastic solutions. Step 1 is a time-marching solution of the aeroelastic problem to proceed from time t to time $t + \Delta t_{AT}$. In step 2 the elastic deformation that occurred during step 1 is passed to the aerothermal model. Step 3 is a time-marching solution of the aerothermal problem to proceed from time t to time $t + \Delta t_{AT}$. Finally, in step 4, the structural temperature distribution is updated in the aeroelastic model.

A.   Aerothermal Solution

The transient temperature distribution in the thermal structure is computed using a finite difference solution to Eq. (11). An explicit scheme with forward-in-time, centered-in-space discretization is used, as shown in Eq. (26). The scheme is first-order-accurate in time and second-order-accurate in space. This simple scheme is selected because the time scale of the heat transfer problem is on the order of seconds, whereas the time scale of the aeroelastic problem is on the order of milliseconds. For the panel investigated, the explicit scheme is numerically stable and highly accurate for aerothermal time steps on the order of 1000 times the aeroelastic time step. Thus, the aerothermal time-step size is limited by the need to update thermal loads in the aeroelastic solution, rather than by the explicit scheme. Therefore, since an explicit formulation is more efficient than an implicit formulation per time step [76], the computational cost of the aerothermoelastic solution is less using an explicit scheme for the aerothermal solution:

$$\rho c \frac{T_{j,i}^{n+1} - T_{j,i}^{n}}{\Delta t} = k_x \frac{T_{j,i+1}^{n} - 2T_{j,i}^{n} + T_{j,i-1}^{n}}{(\Delta x)^2}$$
$$+ k_z \frac{T_{j+1,i}^{n} - 2T_{j,i}^{n} + T_{j-1,i}^{n}}{(\Delta z)^2} \tag{26}$$

Equation (26) is rearranged to Eq. (27) to show the general form of the explicit method used to compute temperature at the new time for an interior node. The form of Eq. (27) is particularly useful for multilayer thermal systems, since it permits variable spacing of nodes and different material properties on each side of the node. The thermal capacitance terms, $\rho c \Delta x$ and $\rho c \Delta z$, are defined in Eq. (28). Half-step indices ($\pm \frac{1}{2}$) are used with the material properties to indicate that the properties are associated with the material between the nodes. Thus, specific heat and thermal conductivity are evaluated

Fig. 7   Aerothermoelastic solution using a partitioned approach to couple aerothermal and aeroelastic solutions.

(and updated every aerothermal time step) using the average temperature of adjacent nodes:

$$T_{j,i}^{n+1} = T_{j,i}^{n} + \frac{k_{j,i+\frac{1}{2}}\Delta t}{(\rho c \Delta x)_{j,i}} \left[\frac{T_{j,i+1}^{n} - T_{j,i}^{n}}{|x_{j,i+1} - x_{j,i}|} \right]$$
$$+ \frac{k_{j,i-\frac{1}{2}}\Delta t}{(\rho c \Delta x)_{j,i}} \left[\frac{T_{j,i-1}^{n} - T_{j,i}^{n}}{|x_{j,i-1} - x_{j,i}|} \right] + \frac{k_{j+\frac{1}{2},i}\Delta t}{(\rho c \Delta z)_{j,i}} \left[\frac{T_{j+1,i}^{n} - T_{j,i}^{n}}{|z_{j+1,i} - z_{j,i}|} \right]$$
$$+ \frac{k_{j-\frac{1}{2},i}\Delta t}{(\rho c \Delta z)_{j,i}} \left[\frac{T_{j-1,i}^{n} - T_{j,i}^{n}}{|z_{j-1,i} - z_{j,i}|} \right] \tag{27}$$

$$(\rho c \Delta x)_{j,i} = (1/2)[(\rho c)_{j,i-\frac{1}{2}}|x_{j,i-1} - x_{j,i}| + (\rho c)_{j,i+\frac{1}{2}}|x_{j,i+1} - x_{j,i}|]$$
$$(\rho c \Delta z)_{j,i} = (1/2)[(\rho c)_{j-\frac{1}{2},i}|z_{j-1,i} - z_{j,i}| + (\rho c)_{j+\frac{1}{2},i}|z_{j+1,i} - z_{j,i}|] \tag{28}$$

The form of Eq. (27) also readily accommodates heat-flux boundary conditions with the aid of Fourier's law of heat conduction and its finite difference approximation given in Eq. (29) [77]. Along the upper surface, which is exposed to aerodynamic heating and thermal radiation, the last term on the right-hand side of Eq. (27) is replaced according to Eq. (30) (for j increasing downward). Adiabatic boundary conditions are also satisfied using Eq. (29) by setting the appropriate term in Eq. (27) to zero:

$$Q_z = -k_z \frac{\partial T}{\partial z} \approx -k_z \frac{\Delta T}{\Delta z} \tag{29}$$

$$\frac{k_{j-\frac{1}{2},i}\Delta t}{(\rho c \Delta z)_{j,i}} \left[\frac{T_{j-1,i}^{n} - T_{j,i}^{n}}{|z_{j-1,i} - z_{j,i}|} \right] = \frac{\Delta t}{(\rho c \Delta z)_{j,i}} [Q_{\text{aero}} - Q_{\text{rad}}]_i^n \tag{30}$$

In this investigation, 21 nodes are used in the chordwise direction and nine nodes (eight elements) are used through the thickness of the panel. Chordwise nodes are evenly spaced. Through-thickness spacing is different for each layer, but uniform within each layer itself. Through-thickness elements are divided as follows: two for the radiation shield, four for the thermal insulation, and two for the plate structure. Thus, the plate structure has a row of nodes located along its upper and lower surfaces and a row at midplate depth.

B.   Aeroelastic Solution

The equation of motion (15) is discretized using Galerkin's method to replace the spatial dependence with a summation of assumed modes [82]. The resulting system of nonlinear ordinary differential equations is integrated directly in the time domain. Homogeneous boundary conditions (geometric and natural) of a simply supported, semi-infinite panel are conveniently satisfied by sine modes [79]. However, inclusion of the thermal moment creates nonhomogeneous natural boundary conditions, Eq. (25). Therefore, the transverse displacement of the panel is assumed to be a summation of sine modes and a third-order polynomial, Eq. (31). Coefficients of the polynomial terms are uniquely defined by satisfying the boundary conditions, while coefficients of the sine modes are determined by carrying out Galerkin's method on the equation of motion:

$$w(x, t) = \sum_{n=1}^{N} A_n \sin \frac{n\pi x}{a} + C_1 + C_2 x + C_3 x^2 + C_4 x^3 \tag{31}$$

To minimize computational effort, the spatial integrations in Galerkin's method are performed analytically before time advancement of the solution. This requires assuming a chordwise dependence for the bending stiffness, Eq. (16), and the thermal moment, Eq. (19). To accomplish this, the discrete temperature distribution in the plate structure is used to evaluate the elastic modulus (using the midplate temperature) and thermal moment at each chordwise node location. The discrete data are then fit by
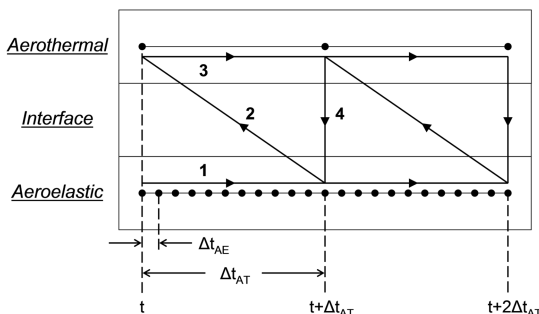
second-order polynomials using the method of least squares. Therefore, the bending stiffness is given by Eq. (32), where E_1, E_2, and E_3 are the fit coefficients. Similarly, the thermal moment is given by Eq. (33), where M_{T1}, M_{T2}, and M_{T3} are the fit coefficients. Note that the thermal moment not only affects the boundary conditions directly, but it also affects the equation of motion through the differential term, $\partial^2 M_T / \partial x^2$. Thus, polynomial representation of second order or higher is required to include the effect of thermal moment in the equation of motion:

$$D(x) = \frac{h^3}{12(1-\nu^2)} (E_1 + E_2 x + E_3 x^2) \qquad (32)$$

$$M_T(x) = M_{T1} + M_{T2}x + M_{T3}x^2 \qquad (33)$$

For convenience, the aeroelastic equations are nondimensionalized. The nondimensional variables are defined as

$$\bar{x} = \frac{x}{a}; \qquad \bar{z} = \frac{z}{h}; \qquad \bar{w} = \frac{w}{h}; \qquad \bar{t} = \frac{t}{\tau}; \qquad \bar{T} = \frac{T}{\Gamma}$$

$$\bar{N}_x = \frac{N_x}{D_0/a^2}; \qquad \bar{N}_T = \frac{N_T}{D_0/a^2}; \qquad \bar{M}_T = \frac{M_T}{D_0 h/a^2}$$

$$\bar{\sigma}_x = \frac{\sigma_x}{\sigma_0}; \qquad \bar{D} = \frac{D}{D_0}; \qquad E_0 = E(T_{\text{ref}}); \qquad \alpha_0 = \alpha(T_{\text{ref}})$$

$$D_0 = \frac{E_0 h^3}{12(1-\nu^2)}; \qquad \sigma_0 = \frac{E_0}{1-\nu^2}\left(\frac{h}{a}\right)^2; \qquad \tau = \left[\frac{\rho_p h a^4}{D_0}\right]^{1/2}$$

$$\lambda = \frac{2q_3 a^3}{M_3 D_0}; \qquad \mu = \frac{\rho_3 a}{\rho_p h}; \qquad \Gamma = \frac{D_0}{E_0 h \alpha_0 a^2} \qquad (34)$$

Substituting the nondimensional variables into Eqs. (1), (15), (19), (22–24), and (32) results in the nondimensional equation of motion provided in Eq. (35) and the corresponding nondimensional terms defined in Eqs. (36–41):

$$\frac{\partial^2}{\partial \bar{x}^2}\left(\bar{D}\frac{\partial^2 \bar{w}}{\partial \bar{x}^2}\right) - \bar{N}_x \frac{\partial^2 \bar{w}}{\partial \bar{x}^2} + \left(\sum_i \frac{\rho_i h_i}{\rho_p h}\right)\frac{\partial^2 \bar{w}}{\partial \bar{t}^2} + \bar{q}_a + \frac{\partial^2 \bar{M}_T}{\partial \bar{x}^2} = 0 \quad (35)$$

$$\bar{D} = \frac{1}{E_0}(E_1 + aE_2\bar{x} + a^2 E_3 \bar{x}^2) \qquad (36)$$

$$\bar{N}_x = \frac{6}{E_0}\left[\int_0^1 \frac{1}{E(\bar{x})}\,d\bar{x}\right]^{-1} \int_0^1 \left(\frac{\partial \bar{w}}{\partial \bar{x}}\right)^2 d\bar{x} - \bar{N}_T \qquad (37)$$

$$\bar{N}_T = \left[\int_0^1 \frac{1}{E(\bar{x})}\,d\bar{x}\right]^{-1} \int_0^1 \frac{\alpha(\bar{x})}{\alpha_0 E_0(1-\nu)} \int_{-1/2}^{1/2} [\bar{T}(\bar{x},\bar{z}) - \bar{T}_{\text{ref}}]\,d\bar{z}\,d\bar{x} \qquad (38)$$

$$\bar{M}_T = \frac{E(\bar{x})\alpha(\bar{x})}{E_0 \alpha_0(1-\nu)} \int_{-1/2}^{1/2}[\bar{T}(\bar{x},\bar{z}) - \bar{T}_{\text{ref}}]\bar{z}\,d\bar{z} = \bar{M}_{T1}$$
$$+ \bar{M}_{T2}\bar{x} + \bar{M}_{T3}\bar{x}^2 \qquad (39)$$

$$\bar{q}_a = \lambda\left[\left(\frac{\mu}{\lambda M_3}\right)^{1/2}\frac{\partial \bar{w}}{\partial \bar{t}} + \frac{\partial \bar{w}}{\partial \bar{x}}\right] + \lambda\left(\frac{h}{a}\right)\frac{\gamma+1}{4}M_3\left[\left(\frac{\mu}{\lambda M_3}\right)^{1/2}\frac{\partial \bar{w}}{\partial \bar{t}}\right.$$
$$\left. + \frac{\partial \bar{w}}{\partial \bar{x}}\right]^2 + \lambda\left(\frac{h}{a}\right)^2\frac{\gamma+1}{12}M_3^2\left[\left(\frac{\mu}{\lambda M_3}\right)^{1/2}\frac{\partial \bar{w}}{\partial \bar{t}} + \frac{\partial \bar{w}}{\partial \bar{x}}\right]^3 \qquad (40)$$

$$\bar{\sigma}_x(\bar{x},\bar{z}) = \frac{\bar{N}_x + \bar{N}_T}{12} - \frac{E(\bar{x})}{E_0}\left[\bar{z}\frac{\partial^2 \bar{w}}{\partial \bar{x}^2}\right]$$
$$- \int_0^1 \frac{E(\bar{x})\alpha(\bar{x})}{12 E_0 \alpha_0(1-\nu)}[\bar{T}(\bar{x},\bar{z}) - \bar{T}_{\text{ref}}]\,d\bar{x} \qquad (41)$$

Next, the nondimensional displacement, Eq. (42), is substituted into Eqs. (35–41). The resulting expression for the nondimensional equation of motion is represented by $\phi(\bar{x},\bar{t})$. Carrying out Galerkin's method, Eq. (43), results in a system of nonlinear second-order ordinary differential equations in time, which is written symbolically in Eq. (44). Note that $\bar{F}_m$ contains products and cross products of the modal amplitudes and modal velocities up to third order. A system of $2N$ first-order differential equations is developed from Eq. (44) using the symbolic formulation given in Eq. (45). Finally, the fourth-order Runge–Kutta method is used to advance this system of equations in the time domain:

$$\bar{w}(\bar{x},\bar{t}) = \sum_{n=1}^N \bar{A}_n \sin(n\pi\bar{x}) + \bar{C}_1 + \bar{C}_2\bar{x} + \bar{C}_3\bar{x}^2 + \bar{C}_4\bar{x}^3 \quad (42)$$

$$\int_0^1 \phi(\bar{x},\bar{t})\sin(m\pi\bar{x})\,d\bar{x} = 0; \qquad m = 1,2,\ldots,N \qquad (43)$$

$$\frac{d^2\bar{A}_m}{d\bar{t}^2} = \bar{F}_m\left(\bar{A}_n, \frac{d\bar{A}_n}{d\bar{t}}\right); \qquad m,n = 1,2,\ldots,N \qquad (44)$$

$$\frac{d\bar{A}_m}{d\bar{t}} = \bar{Y}_m; \qquad \frac{d\bar{Y}_m}{d\bar{t}} = \bar{F}_m \qquad (45)$$

Previous panel flutter investigations [29,38,79] have demonstrated that six modes in the flow direction produce converged flutter solutions; thus, six sine modes are used in this study. Spatial integrations involving discrete temperature and material property distributions are performed numerically using the trapezoidal rule [83]. Temperature distributions, material properties, and the polynomial coefficients in Eqs. (36), (39), and (42) are updated every aerothermal time step.

IV.   Results and Discussion

To the authors' knowledge, no data exist to validate the developed aerothermoelastic model. Therefore, steps to verify the model are carried out for the aerothermal and aeroelastic models individually. Note that the aerothermal model is verified in two parts: 1) aerodynamic heating and 2) heat transfer.

In addition to performing model verifications, the aerothermoelastic model is used to investigate the effects of various types of fluid–thermal–structural coupling on flutter boundary prediction, nonlinear flutter response, and dynamically stable response of a panel in hypersonic flow. Furthermore, the effects of the different types of coupling on the accuracy and the computational expense of the aerothermoelastic solution are investigated.

A.   Aerothermal Model Verification

1.   Aerodynamic Heating

The present aerodynamic pressure and heating models are compared to experimental results [84] from investigations conducted on flat plates and spherical dome protuberances in the NASA Langley Research Center's 8-Foot High-Temperature Tunnel (HTT). The HTT is a hypersonic blowdown tunnel that can simulate aerodynamic pressure and heating obtained in flight at a nominal Mach number of 7 in the altitude range between 25 and 40 km for up to 2 min, depending on test conditions [84–86]. The high-energy required to simulate hypersonic flow conditions is obtained by burning a mixture of methane and air under pressure and expanding the combustion products to the test-section Mach number. Thus, in order to compare pressure and heating predictions from the present formulation with the experimental data [84], thermodynamic and transport properties of methane–air combustion products [87] must be used.

Analytical predictions of aerodynamic pressure and heating for an inclined flat-plate test article were made in [85] using oblique shock

Table 2   Flat-plate validation of the present aerodynamic pressure and heating models by comparison to experimental data [84]

	Input				Output			
Experimental vs analytical	p_∞ Pa	T_∞ K	M_∞	θ deg	p_{fp} Pa	% error	Q_{fp} W/cm^2	% error
Run 30 (NASA TP-2631 [84])	654.9	——	6.60	5.0	1278	——	4.783	——
Present ($R_{eq} = 0.9$)	654.9	220.0	6.60	5.0	1390	8.8	5.225	9.3
Run 31 (NASA TP-2631 [84])	648.0	——	6.60	5.0	1275	——	4.764	——
Present ($R_{eq} = 0.9$)	648.0	220.0	6.60	5.0	1376	7.9	5.181	8.7
Run 32 (NASA TP-2631 [84])	654.9	——	6.60	5.0	1278	——	4.555	——
Present ($R_{eq} = 0.9$)	654.9	220.0	6.60	5.0	1390	8.8	5.225	14.7

Table 3   Diameter and height of the spherical pressure (PD) and heat-flux (TD) domes used in aerothermal tests [84]

	Spherical dome protuberances					
	D_{dome}		H_{PD}		H_{TD}	
Test ID	in.	m	in.	mm	in.	mm
Run 30	14.0	0.356	0.390	9.91	0.465	11.8
Run 31	14.0	0.356	0.182	4.62	0.179	4.55
Run 32	14.0	0.356	0.090	2.29	0.144	3.66

relations [61] and Eckert's reference temperature method [64] with the properties of methane–air combustion products [87]. Thus, Eckert's reference temperature method was used (instead of Eckert's reference enthalpy method) in the present formulation in order to verify modifications for methane–air combustion products by direct comparison to the analytical results in [85] before performing the present validation study with [84]. Furthermore, due to a lack of the necessary temperature-enthalpy tables for methane–air combustion products required by Eckert's reference enthalpy method, Eckert's reference temperature method is used for the present validation study. Note that Eckert's reference temperature method has been shown to overpredict aerodynamic heating on the order of 10% compared to Eckert's reference enthalpy method for Mach 8 flow at an altitude of 30 km [88].

In addition to using the properties of methane–air combustion products, several assumptions are required in order to compute pressure and heat-flux values with the present models, since the equivalence ratio, the freestream temperature, and the wall temperature are not reported in [84]. First, an equivalence ratio of 0.9 is selected from those available (0.7, 0.8, 0.9, and 1.0) in [87], based on the HTT operating conditions reported in [84–86]. Second, the freestream temperature is based on the local stream temperatures reported in [85] for zero-inclination angle tests that have HTT

operating conditions similar to those in [84]. Third, a wall temperature of 300 K is assumed, since the heating rates are reported [84] to be for a cold wall. Finally, flat-plate heat-flux values from the present model are computed at a distance 1.85 m downstream of the onset of transition, which is the distance from the boundary-layer trips to the center of the test article [84].

In this validation study, two comparisons are made to the experimental data contained in [84]. The first is for flat plates and the second is for spherical dome protuberances. In both experimental configurations, the test article is mounted on a flat plate (panel holder), which has a sharp leading edge and is inclined to the flow [84].

Table 2 contains a summary of the results from the flat-plate validation study. The output columns of Table 2 illustrate that the present models predict flat-plate pressure values between +7.9% and +8.8% and heat-flux values between +8.7% and +14.7% of the experimental values reported in [84]. These errors are within the ranges anticipated, considering the number of assumptions required, and the error ranges reported [85] for the analytical methods used (compared to the experimental data [85], average pressure ratios were predicted within ±10% and average turbulent heating rates were overpredicted from 10 to 30%).

Next, the present formulation is compared to experimental pressure and heating results for spherical dome protuberances [84]. Table 3 lists the diameter and height of the spherical dome protuberances used in the sharp leading-edge panel-holder test cases [84]. Note that the pressure and heat-flux domes have equal diameters that are the same for each test, but the domes have different heights with respect to each other and different heights for each test. Also, as listed in Table 2, each test was performed with similar freestream conditions and at the same flat-plate (panel-holder) inclination angle.

Figures 8a and 8b compare pressure and heating predictions over the streamwise centerline of the spherical dome protuberances from the present models to the experimental data [84], respectively.

a) Streamwise centerline pressure distributions

b) Streamwise centerline heating distributions
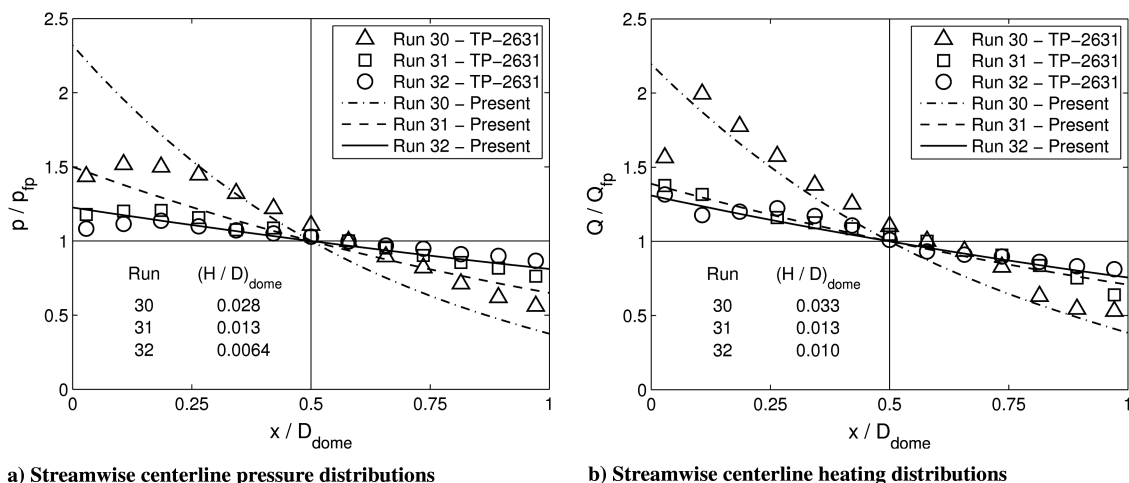
Fig. 8   Pressure and heating distributions from the present models compared to experimental data along the streamwise centerline of spherical dome protuberances [84].

Table 4   Maximum and average absolute error of pressure and heating distributions from the present models compared to experimental data along the streamwise centerline of spherical dome protuberances [84]

| | % error | | | | | |
| | Run 30 | | Run 31 | | Run 32 | |
Absolute error	p/p_{fp}	Q/Q_{fp}	p/p_{fp}	Q/Q_{fp}	p/p_{fp}	Q/Q_{fp}
Max	54.5	34.6	24.4	13.1	11.9	7.1
Avg	18.6	13.1	9.3	3.8	3.7	3.6

Pressure and heating distributions are normalized by the corresponding flat-plate results provided in Table 2. Note that the leading edge of each dome is at $x/D_{dome} = 0$ and the trailing edge is at $x/D_{dome} = 1$. The analytical results and the experimental data show that pressure and heating are increased in the leading-edge region and decreased in the trailing-edge region compared to the flat-plate values. In addition, these effects increase with increasing dome height.

Maximum and average absolute values of the error from the present models relative to the experimental data are listed in Table 4. The maximum error values occur near the leading edge, as illustrated in Figs. 8a and 8b. The errors are greater for pressure than for heating, and increase with increasing dome height. The average error values illustrate that pressure and heating predictions from the present models are in general agreement with the experimental data. The average absolute error of the pressure distribution predictions is between 3.7 and 18.6%, and the average absolute error of the heating distribution predictions is between 3.6 and 13.1%. Thus, the present aerothermodynamic model yields reasonable agreement with experimental heating distributions over spherical dome protuberances.
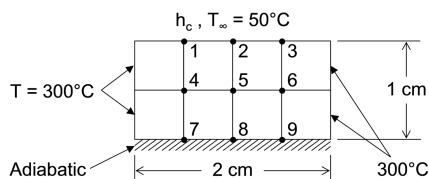
2. Heat Transfer

The present heat transfer model is verified by computing the two-dimensional transient temperature distribution in the ceramic strip shown in Fig. 9. A solution to this problem is provided in example 4-12 of [77]. The ceramic strip is initially at a uniform temperature of 300°C, and at time zero it is exposed to convective cooling along the upper surface. Convective cooling is modeled using a convection heat transfer coefficient and the fluid temperature, as given by Eq. (46). The convection heat transfer coefficient and material properties are listed in Table 5. The sides of the ceramic strip are maintained at 300°C and the lower surface is adiabatic:

$$Q_{conv} = h_c(T_\infty - T_w) \qquad (46)$$

Transient temperature values of node 5 from [77] and from the present model are compared in Table 6. Note that [77] uses a time step of $\Delta t = 2.0$ s, based on the maximum time step ($\Delta t = 2.286$ s) for numerical stability of the explicit scheme for this problem. Solutions from the present model are provided at $\Delta t = 2.0, 0.2$, and 0.02 s. The solution at $\Delta t = 2.0$ s is used to verify the present model by comparison to [77]. Solutions at $\Delta t = 0.2$ and 0.02 s demonstrate convergence of transient nodal temperatures for $\Delta t = 0.2$ s.

B. Aeroelastic Model Verification

The present aeroelastic model is verified by comparison to stability-region boundaries in [79] and to the limit cycle amplitudes in [44,79]. Dowell [79] used an analytical time-domain model with

Fig. 9   Two-dimensional transient heat transfer example 4-12 of [77].

Table 5   Heat transfer verification parameters from example 4-12 of [77]

h_c	200	W/m^2/K
ρ	1600	kg/m^3
c	800	J/kg/K
k	3.0	W/m/K

Table 6   Comparison of node 5 temperature (°C) from example 4-12 of [77]

Time, s	Holman [77] $\Delta t = 2.0$	Present $\Delta t = 2.0$	Present $\Delta t = 0.2$	Present $\Delta t = 0.02$
0.0	300.0	300.0	300.0	300.0
2.0	300.0	300.0	297.9	297.8
4.0	294.1	294.1	293.4	293.3
6.0	287.6	287.6	288.3	288.4
8.0	282.4	282.4	283.5	283.6
10.0	277.8	277.8	279.2	279.3
12.0	274.0	274.0	275.4	275.5

quasi-steady, linear supersonic aerodynamic theory and six sine modes to investigate a simply supported, semi-infinite panel under the influence of applied, in-plane mechanical load. Xue and Mei [44] used a finite element frequency-domain model with first-order (linear) piston theory to examine the same panel under in-plane thermal load. Note that the present formulation uses third-order (nonlinear) piston theory, which has dependence on an additional nondimensional parameter: $(h/a)M_3$, Eq. (40), compared to the linear theories used in [44,79]. Thus, for model verification, first-order piston theory is employed. Also, in the present model and in [44], an in-plane thermal load caused by a uniform temperature rise ΔT is modeled in an equivalent manner to an applied in-plane mechanical load R_x from [79]. In nondimensional form, the critical value of in-plane compressive load that causes buckling is π^2. Therefore, denoting the critical uniform temperature rise that causes buckling by ΔT_{cr}, the relationship $\Delta T/\Delta T_{cr} = -R_x/\pi^2$ is used to compare results from the present model and from [44] to [79].

Figure 10a shows close agreement between the stability-region boundaries given in [79] and stability-boundary data points from the present model. Stability-boundary data points are identified by specifying the dynamic pressure and the in-plane thermal load and then examining the transient response. Examples of typical transient response in each stability region are given in [29]. It is important to note that the regions *flat and stable* and *buckled but dynamically stable* do not involve oscillations, whereas regions *limit cycle oscillation (simple harmonic)* and *limit cycle oscillation (periodic, but not simple harmonic)* involve self-excited, self-sustained oscillations: i.e., nonlinear panel flutter. Therefore, the flutter boundary is defined by line segments *A-B* and *B-C* in Fig. 10a. Regions to the left and below the flutter boundary (line *A-B-C*) are dynamically stable, whereas regions to the right and above line *A-B-C* involve limit cycle flutter.

Figure 10b compares the peak amplitudes of limit cycle oscillation from the present model to [44,79] at four values of in-plane thermal load ($\Delta T/\Delta T_{cr} = 0, 1, 2, 3$). Data from the present model are in close agreement with both sets of reference data.

C. Aerothermoelastic Panel Studies

The aerothermoelastic model is used to investigate the impact of fluid–thermal–structural coupling on aerothermoelastic behavior: i.e., on flutter boundary predictions, nonlinear flutter response, and dynamically stable response. Multiple important effects are included in the analysis: namely, 1) mutual coupling between elastic deformation and aerodynamic heating (i.e., two-way coupling), 2) transient arbitrary in-plane and through-thickness temperature distributions, and 3) the associated thermal stresses and material property degradations. Furthermore, two simplified approaches are
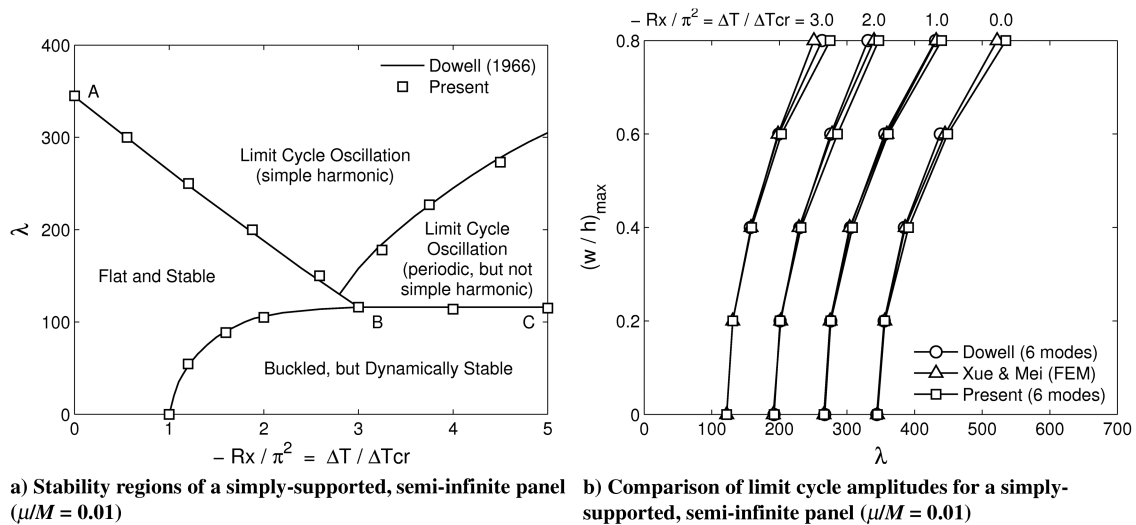
a) Stability regions of a simply-supported, semi-infinite panel ($\mu/M = 0.01$)

b) Comparison of limit cycle amplitudes for a simply-supported, semi-infinite panel ($\mu/M = 0.01$)

Fig. 10   Aeroelastic model verification study [44,79].

investigated for reducing the computational expense of aerother-moelastic analysis in hypersonic flow: specifically, 1) quasi-static coupling and 2) time-averaged dynamic coupling of aerothermal and aeroelastic solutions.

1. Aerothermoelastic Modeling Cases

Table 7 lists eight modeling cases (*B*-1, *B*-2, *C*-1, *C*-2, *D*-1, *D*-2, *E*-1, and *E*-2) considered in the present study. All cases include transient arbitrary in-plane and through-thickness temperature distributions, and the associated thermal stresses. Cases *B*-1 and *B*-2 neglect material property degradation; *B*-1 uses one-way coupling (aeroheating based on the undeformed panel) and *B*-2 uses two-way coupling (aeroheating based on the deformed panel). Cases *C*-1 and *C*-2 include material property degradation due to temperature change, but are otherwise equivalent to *B*-1 and *B*-2, respectively. Note that these four cases (*B*-1, *B*-2, *C*-1, and *C*-2) use a quasi-static formulation of the structural model and thus quasi-static coupling.

The quasi-static formulation neglects the velocity and acceleration terms in Eq. (44); thus, the system of nonlinear differential equations of motion, becomes a system of nonlinear algebraic equations of equilibrium. These equations are solved iteratively, using the Levenberg–Marquardt algorithm [89], to update the quasi-static deformation each time the temperature is updated from the transient aerothermal solution. To identify the aerothermoelastic flutter boundary, dynamic response tests are performed on the quasi-static solutions. The onset of flutter (i.e., flutter boundary) is defined as the first point in time along a trajectory that sustained oscillations are predicted by the dynamic response test.

The latter four cases (*D*-1, *D*-2, *E*-1, and *E*-2) use the dynamic formulation of the structural model. Cases *D*-1 and *D*-2 are the dynamic versions of *C*-1 and *C*-2, respectively. Note that the first six cases (*B*-1, *B*-2, *C*-1, *C*-2, *D*-1, and *D*-2) use equal time steps for the aerothermal and aeroelastic solutions. However, cases *E*-1 and *E*-2 use multiple aeroelastic time steps for each aerothermal time step,

and thus are simplified versions of *D*-1 and *D*-2, respectively. Case *E*-2 computes the aerodynamic heating from the time-averaged dynamic response over multiple aeroelastic time steps. This enables different time steps for the aerothermal and aeroelastic solutions within the two-way coupled framework. All other cases that implement two-way coupling (*B*-2, *C*-2, and *D*-2) use equal time steps; thus, the instantaneous panel deformation is used to compute aerodynamic heating. Finally, note that case *D*-2 is the baseline for this study, since all other cases use one or more simplifications of the complete aerothermoelastic model.

2. Aerothermoelastic Flutter Boundary Predictions

Hypersonic aerothermoelastic analysis is challenging due to transient thermal stresses, material properties, and aerodynamic heating conditions. Therefore, unlike other flow regimes where aeroelasticity is primarily dependent on instantaneous operating conditions, hypersonic aerothermoelasticity is dependent on the path between two points [60]. Thus, flight trajectory, time, and transient heat transfer analysis become essential components to accurate aerothermoelastic flutter boundary prediction. In this study, the aerothermoelastic flutter boundary is computed by marching the aerothermal and aeroelastic equations forward in time for a specified set of trajectories and initial conditions. The only variation of trajectory considered is Mach number; thus, both altitude and angle of attack are held constant.

The parameters used in this investigation are listed in Table 8. Panel layer thicknesses are given above in Table 1. The panel is initially flat, stress-free, and at a uniform temperature.

Figure 11a shows a comparison of the aerothermoelastic flutter boundaries as a function of Mach number and flight time for each modeling case. Note that the unheated flutter boundary for this panel is $M_\infty = 18.3$. The effect of thermal stresses, in the absence of material property degradation, on lowering the unheated flutter boundary is illustrated by cases *B*-1 and *B*-2. Furthermore, when material property degradation is included (*C*-1, *C*-2, *D*-1, *D*-2, *E*-1, and *E*-2) the flutter boundary is further reduced. Note that the error

Table 7   Aerothermoelastic modeling cases

Case	Material property degradation	Aerothermal-aeroelastic coupling	Aeroheating panel deformation	Structural model formulation
B-1	None	1-way	Undeformed	Quasi-static
B-2	None	2-way	Instantaneous	Quasi-static
C-1	$E(T), \alpha(T)$	1-way	Undeformed	Quasi-static
C-2	$E(T), \alpha(T)$	2-way	Instantaneous	Quasi-static
D-1	$E(T), \alpha(T)$	1-way	Undeformed	Dynamic
D-2	$E(T), \alpha(T)$	2-way	Instantaneous	Dynamic
E-1	$E(T), \alpha(T)$	1-way	Undeformed	Dynamic
E-2	$E(T), \alpha(T)$	2-way	Time-averaged	Dynamic

Table 8   Parameters used to investigate aerothermoelastic flutter boundary predictions

Altitude	30 km
M_∞	7.5–12
θ	5.0°
x_3	1.0 m
a	1.5 m
h	5.0 mm
$T_{initial}$	300 K

a) Flutter boundaries for the aerothermoelastic
modeling cases

b) Flight time to the onset of flutter at select M_∞ trajectories
for the aerothermoelastic modeling cases that include
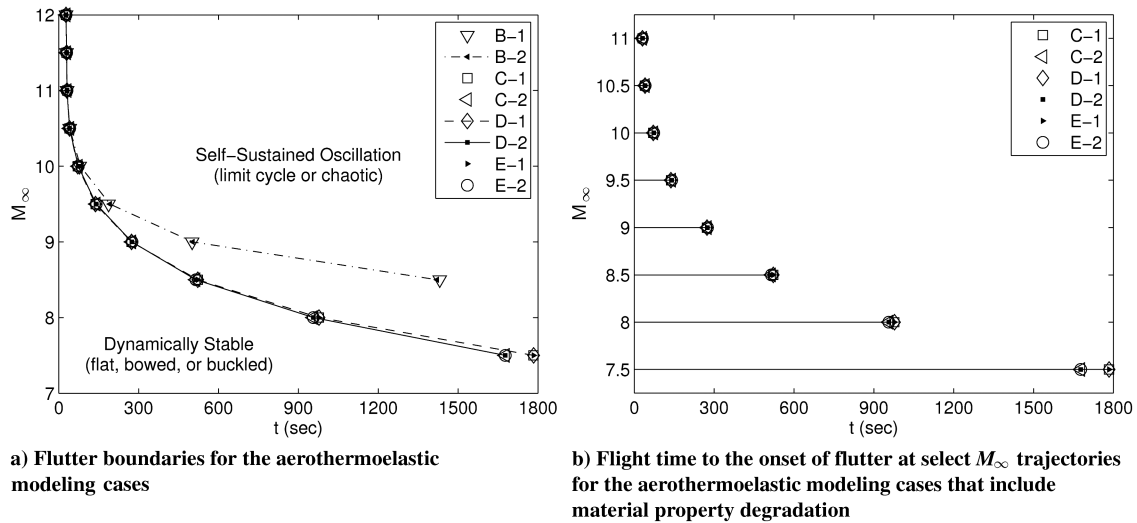material property degradation

Fig. 11   Aerothermoelastic flutter boundary predictions.

introduced by neglecting material property degradation increases with decreasing Mach number (i.e., the error increases with increasing flight time to reach the flutter boundary). For the $M_\infty = 8.5$ trajectory (the lowest Mach number considered for cases B-1 and B-2), flight time to reach the flutter boundary is overpredicted by approximately 180%, due to neglecting material property degradation.

Another significant result shown in Fig. 11a is general agreement in flutter boundary predictions between one-way coupling (C-1, D-1, and E-1) and two-way coupling (C-2, D-2, and E-2) when material property degradation is included. However, at the lower Mach numbers considered, a difference between one-way and two-way coupling is evident. This is best illustrated by comparing flight time to the onset of flutter for each trajectory, as shown in Fig. 11b. Note that the differences in the flutter boundary predictions increase with decreasing Mach number; the largest difference occurs at $M_\infty = 7.5$ (the lowest Mach number considered). For this trajectory, the one-way coupled cases (C-1, D-1, and E-1) overpredict flight time to the onset of flutter by 6.3% compared to the two-way coupled cases (C-2, D-2, and E-2).

Finally, note that these results are configuration-dependent, since the degradation of material properties depends on the structural material and transient heat transfer through the TPS. Furthermore, panel length and thickness impact the amplitude of preflutter buckling, and thus the degree to which deformation, flow, and heating are coupled before flutter. More complex aerodynamic theories are needed, however, to investigate additional configurations that exhibit larger preflutter deformations, since piston theory is limited by the product of Mach number and surface inclination [53].

3. Aerothermoelastic Solution Considerations

Note from Figs. 11a and 11b that there is excellent agreement between the C, D, and E cases. This indicates that the aerothermoelastic behavior of the panel can be accurately represented using either quasi-static or time-averaged dynamic fluid–thermal–structural coupling. To further evaluate these solution strategies,

consider the solution time parameters for the aerothermoelastic modeling cases provided in Table 9. Note that for cases C-1 and C-2, the time-step size is limited by the aerothermal solution. Conversely, the time-step size for cases D-1 and D-2 is limited by the dynamic aeroelastic solution. Cases E-1 and E-2 use the aerothermal time step from C-1 and C-2 and the aeroelastic time step from D-1 and D-2. Note that time-step sizes for the aerothermal and aeroelastic solutions are determined from independent time-step convergence studies of each solution, respectively.

The computational expense of each case is represented in Table 9 as CPU time/flight time. It is interesting that the computational cost of cases C-1 and C-2 are the same, as is the cost of cases D-1 and D-2, and E-1 and E-2. Thus, for the model developed, there is no additional expense associated with two-way coupling of the aerothermoelastic solution.

Next, note that the computational expense of cases C-1 and C-2 (quasi-static coupling) is approximately 0.7% of D-1 and D-2 (dynamic coupling with equal aerothermal and aeroelastic time steps). Furthermore, cases E-1 and E-2 (time-averaged dynamic coupling with different aerothermal and aeroelastic time steps) are approximately 9% of D-1 and D-2. Thus, both quasi-static and time-averaged dynamic coupling result in significant increases in computational efficiency of the aerothermoelastic solution.

Finally, the division of computational expense between the aerothermal and aeroelastic solutions is listed under CPU time in Table 9. The aerothermal solution accounts for approximately 70% of the computational cost of cases C-1 and C-2 and 92% of D-1 and D-2. However, for cases E-1 and E-2, the aerothermal solution accounts for only 5% of the cost. Thus, the high-cost of the instantaneous dynamic coupling cases (D-1 and D-2) is primarily due to solving the aerothermal problem on the same time scale as the aeroelastic solution.

4. Nonlinear Aerothermoelastic Flutter Response

A principal consideration for an aerothermoelastic analysis, in addition to flutter prediction, is the ability to accurately capture dynamic aerothermoelastic response phenomena. This is assessed in the present study by investigating the nonlinear aerothermoelastic panel flutter response for the $M_\infty = 10$ and 10.5 trajectories using the dynamic cases D-1, D-2, E-1, and E-2. The $M_\infty = 10$ trajectory shows a response in which the panel is buckled for a significant period of time before flutter, whereas for the $M_\infty = 10.5$ trajectory, the onset of flutter occurs shortly after buckling. Note that as Mach number decreases, the duration of buckled but dynamically stable response before the onset of flutter increases. During this period of time, buckling deformations increase due to aerodynamic heating. At Mach numbers lower than 9.5, the panel experiences relatively large amplitude oscillations immediately following the onset of flutter,

Table 9   Aerothermoelastic solution time parameters

Case	Aerothermal time step, ms	Aeroelastic time step, ms	CPU[a] time/flight time, s/s	CPU[a] time, %
C-1	100	100	3.6	70 AT, 30 AE
C-2	100	100	3.6	70 AT, 30 AE
D-1	0.5	0.5	540	92 AT, 8 AE
D-2	0.5	0.5	540	92 AT, 8 AE
E-1	100	0.5	47	5 AT, 95 AE
E-2	100	0.5	47	5 AT, 95 AE

[a]One 2.6 GHz Opteron processor, 2.0 GB RAM.

a) Displacement envelope ($M_\infty = 10$)

b) Onset of flutter ($M_\infty = 10$)

c) Limit cycle oscillations ($M_\infty = 10$)
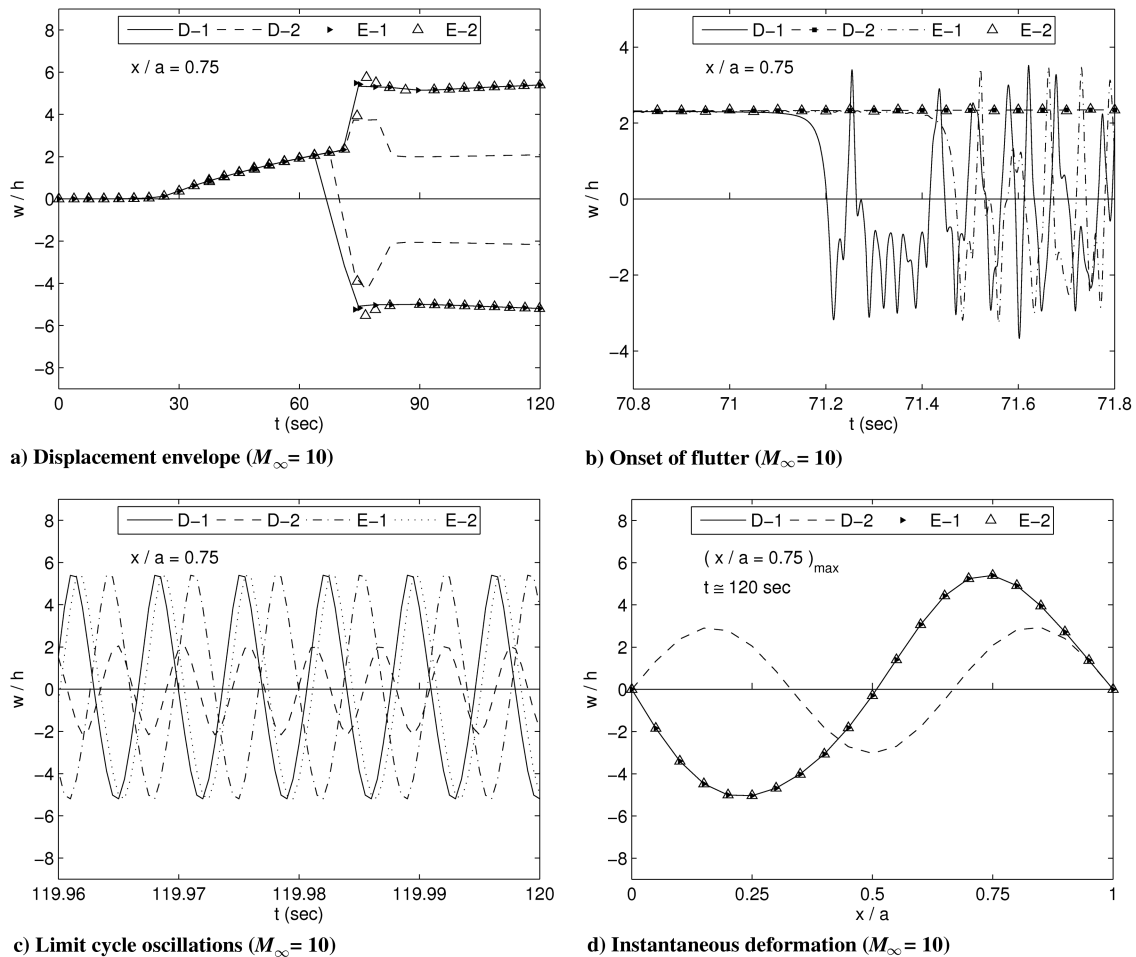
d) Instantaneous deformation ($M_\infty = 10$)

Fig. 12   Nonlinear aerothermoelastic panel flutter response at $M_\infty = 10$.

due to the large preflutter buckling deformations. The flutter oscillations are large enough that in some instances piston theory computes a fictitious negative value of the instantaneous pressure, due to overexpansion of the flow. Thus, additional work is needed to confirm the accuracy of the postflutter responses at the lower Mach numbers using more sophisticated aerodynamic tools.

The aerothermoelastic responses for the $M_\infty = 10$ and 10.5 trajectories are represented in Figs. 12a–12c and 13a–13c, respectively, using the transient panel displacements at the 0.75-chord location. Peak displacements generally occur near this location, since the majority of the flutter responses are dominant in the second mode, as shown in Figs. 12d and 13d. The displacement envelopes are illustrated in Figs. 12a and 13a. Four distinct regions of response are evident: namely, 1) initially flat and stable, followed by 2) buckled but dynamically stable deformation, before 3) the onset of flutter and a transition to 4) steady limit cycle oscillations. The onset of flutter is presented in Figs. 12b and 13b, and the limit cycle oscillations are shown in Figs. 12c and 13c. Note that the time scale in Figs. 12b, 12c, 13b, and 13c is reduced compared to Figs. 12a and 13a in order to clearly discern the oscillations. In all cases, the transition to steady flutter is preceded by a period of chaotic snap-through motion. Note that this behavior is also described for forced motion of buckled beams in [90].

An interesting difference between the baseline case (D-2) and the cases which involve one or more model simplifications (D-1, E-1, and E-2) is illustrated in Figs. 12a–12d for the $M_\infty = 10$ trajectory. First, it is evident in Figs. 12c and 12d that mode 2 is dominant for D-1, E-1, and E-2, whereas mode 3 is dominant for D-2 during limit cycle oscillations. The corresponding frequencies are approximately 140 Hz and 180 Hz, respectively. Next, note in Fig. 12a that in the buckled but dynamically stable region (25–70 s), the four responses are in close agreement; the responses in this region are dominant in

the first and second modes. At the onset of flutter (approximately 71 s), mode 2 becomes dominant for each response, which is evident by the sharp increase in amplitude at the 0.75-chord location. However, during the transition to limit cycle oscillations (72–85 s), D-2 predicts a switch to mode 3 (evident by the sharp decrease in displacement at approximately 80 s), while the other cases remain in mode 2. It is interesting to note that since case E-2 uses time-averaged deformation to implement two-way coupling, postflutter oscillations about the flat panel configuration result in aerodynamic heat loads similar to one-way coupling (D-1 and E-1). Therefore, these results suggest that the flutter response may be altered by the mutual coupling of panel oscillations and aerodynamic heating, an effect captured only by case D-2 in this study.

Conversely, Figs. 13a–13d illustrate that the aerothermoelastic responses predicted by all four cases (D-1, D-2, E-1, and E-2) are in close agreement for the $M_\infty = 10.5$ trajectory. For each case, the steady limit cycle oscillations are dominant in the second mode (approximately 140 Hz) as illustrated in Figs. 13c and 13d. One significant difference between the response at $M_\infty = 10.5$ and the response at $M_\infty = 10$ is the duration of the buckled but dynamically stable region and the corresponding deformation at the onset of flutter. At $M_\infty = 10.5$, the panel is buckled for a shorter period of time (approximately 15 s compared to 45 s) and thus is deformed less ($w/h = 1.0$ compared to $w/h = 2.3$) at the onset of flutter. Therefore, the impact of two-way coupling at the onset of flutter and early in the flutter response is less significant at $M_\infty = 10.5$ than at $M_\infty = 10$.

Collectively, the $M_\infty = 10$ and 10.5 results suggest that dynamic aerothermoelastic response is sensitive to both the level of coupling (one-way versus two-way) and to temporal coupling (time-averaged versus instantaneous). However, since time-averaged two-way coupling (E-2) and one-way coupling (D-1 and E-1) produce

a) Displacement envelope ($M_\infty = 10.5$)

b) Onset of flutter ($M_\infty = 10.5$)

c) Limit cycle oscillations ($M_\infty = 10.5$)
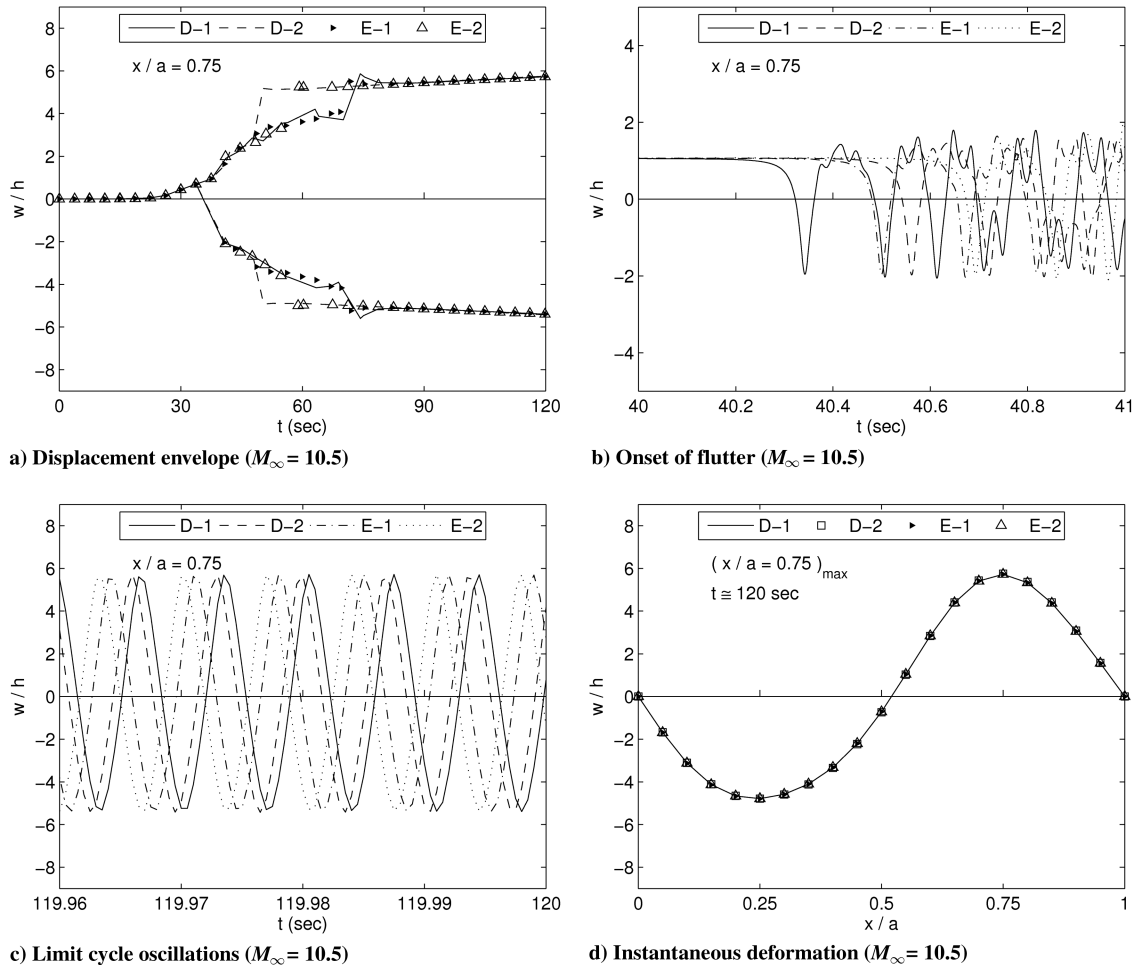
d) Instantaneous deformation ($M_\infty = 10.5$)

Fig. 13 Nonlinear aerothermoelastic panel flutter response at $M_\infty = 10.5$.

accurate results compared to the baseline model (D-2) for some responses, additional work is needed to fully characterize their use.

5. Dynamically Stable Aerothermoelastic Response

Another important consideration for an aerothermoelastic analysis is the ability to accurately capture dynamically stable responses: e.g., quasi-static elastic deformation and buckling. To investigate this behavior, aerothermoelastic responses in the preflutter region of the $M_\infty = 8.0$ trajectory are investigated using one-way (C-1 and D-1) and two-way (C-2 and D-2) coupled solutions. Comparison of the quasi-static coupling cases (C-1 and C-2) to the dynamic coupling cases (D-1 and D-2) is performed to investigate the accuracy of quasi-static coupling. This trajectory is selected because flight time in the preflutter region is greater than at higher Mach numbers (see Fig. 11). Additionally, at $M_\infty = 8.0$ the one-way coupled and two-way coupled flutter boundary predictions begin to separate; thus, the preflutter response parameters that lead to this separation are of interest.

The panel deformation, heating, material property degradation, thermal loading, and stress results from this investigation are presented in three sets of figures: Figs. 14a–14d, 15a–15d, 16a, and 16b. Figure 14a illustrates the initially flat panel and the buckled but dynamically stable panel deformations at 300 and 900 s. Panel deformations from each of the four cases are in close agreement, indicating that the elastic deformation does not have a strong dependence on the coupling procedure used.

Aerodynamic heat-flux distributions over the panel at the initial time, 300 s, and 900 s are shown in Fig. 14b. The values of aerodynamic heat flux are lower at 300 and 900 s compared to the initial time, due to increasing surface temperatures. The quasi-static coupling cases C-1 and C-2 are in close agreement with the dynamic

coupling cases D-1 and D-2, respectively. However, the difference between one-way coupling (C-1 and D-1) and two-way coupling (C-2 and D-2) increases with time. At 900 s, aerodynamic heat flux is approximately 52% greater at 0.35 chord and 79% less at the trailing edge for cases C-2 and D-2 compared to C-1 and D-1.

Figure 14c illustrates the aerodynamic surface temperature at 10 s, 300 s, and 900 s. For cases C-1 and D-1 (one-way coupling), the surface temperature is the same at 300 and 900 s (approximately 1170 K and uniform); this is approximately the flat-plate radiation equilibrium temperature. The surface temperature change from the initial value of 300 K to approximately 1020 K at 10 s indicates that the equilibrium surface temperature is reached rapidly for one-way coupling. However, cases C-2 and D-2 (two-way coupling) predict that surface temperature continues to change throughout the trajectory. The temperature rise at 900 s is approximately 15% greater at 0.35 chord and 43% less at the trailing edge for cases C-2 and D-2 compared to C-1 and D-1. These results demonstrate that in hypersonic flow, deforming panels may not exhibit a radiation equilibrium wall temperature, and that two-way coupling is required in order to accurately predict material temperatures at the surface.

Midplate temperature distributions at the initial time, 300 s, and 900 s are shown in Fig. 14d. The temperature distributions are uniform, 300 K, at the initial time for each case. At 300 s, the midplate temperatures are approximately 400 K. However, for cases C-2 and D-2 (two-way coupling) the temperature rise is slightly greater at the leading edge and less at the trailing edge than for C-1 and D-1 (one-way coupling). At 900 s, the midplate temperature distribution for case C-1 and D-1 is nearly uniform with 580 K at the leading edge and 560 K at the trailing edge. In contrast, the temperature rise shown by C-2 and D-2 is approximately 18% greater at 0.35 chord and 33% less at the trailing edge compared to C-1 and D-1. It is interesting to note that the midplate temperature profiles (Fig. 14d) follow the

a) Panel deformation at time zero, 300 sec, and 900 sec

b) Aerodynamic heat flux at time zero, 300 sec, and 900 sec

c) Aerodynamic surface temperature at 10 sec, 300 sec, and 900 sec

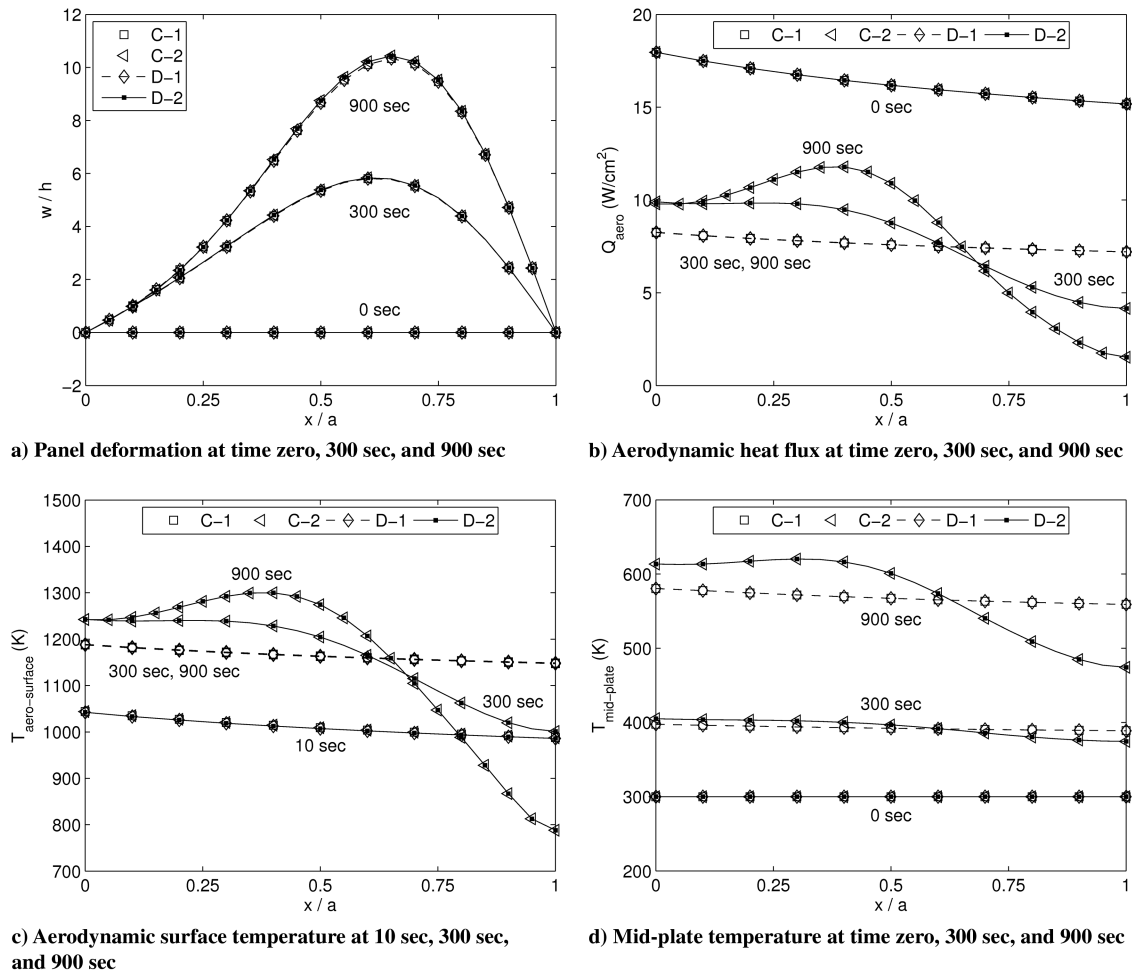d) Mid-plate temperature at time zero, 300 sec, and 900 sec

Fig. 14   Panel deformation and heating during dynamically stable aerothermoelastic response at $M_\infty = 8.0$.

aerodynamic surface temperature profiles (Fig. 14c), where the time lag is due mainly to the thermal insulation between them. From these results it is clear that elastic deformation of a structure can significantly affect its internal temperature distribution.

Figure 15a illustrates the normalized elastic modulus of the plate structure at the initial time, 300 s, and 900 s. The values are based on the midplate temperature distributions in Fig. 14d. Since the elastic modulus decreases as the temperature increases, the inverse trend is shown in Fig. 15a compared to Fig. 14d. At 900 s, the elastic modulus from cases C-1 and D-1 (one-way coupling) is nearly uniform and is approximately 87% of its value at time zero. However, the elastic modulus from cases C-2 and D-2 (two-way coupling) is approximately 2.3% less at 0.35 chord and 4.3% greater at the trailing edge compared to C-1 and D-1. This demonstrates the importance of two-way coupling for evaluating material property degradation at elevated temperature.

Transient in-plane thermal force, normalized by the critical buckling load, is illustrated in Fig. 15b. All four cases (C-1, C-2, D-1, and D-2) are in close agreement. This is due to the dependence of in-plane thermal force on the integral of temperature distribution (Fig. 14d) over the length of the panel. Thus, in-plane thermal forces computed from one-way and two-way coupling are nearly identical because the average temperatures of the plate structure are approximately the same.

Note that the main parameters which influence the flutter boundary predictions (Fig. 11) are 1) deformation induced pressure, 2) panel stiffness, and 3) in-plane thermal force. The preflutter buckling deformations (Fig. 14a) and the in-plane thermal forces (Fig. 15b) are nearly identical for all four cases. This suggests that separation of one-way and two-way coupled flutter boundary predictions, which begins to occur at $M_\infty = 8.0$, is a result of different panel stiffnesses due to variation of the elastic modulus (Fig. 15a). Moreover,

agreement of C-1 with D-1 and C-2 with D-2 for each of these parameters in the preflutter region further justifies use of the quasi-static coupling procedure for flutter boundary prediction.

The thermal bending moment at the initial time, 300 s, and 900 s is shown in Fig. 15c. Note that the thermal bending moment is greater at 300 s than at 900 s, since the through-thickness thermal gradients are largest at earlier times. In addition, the nonuniform aerodynamic heating that results from two-way coupling (C-2 and D-2) produces steeper temperature gradients at the leading edge and shallower gradients at the trailing edge. Consequently, at 900 s, the thermal bending moments for cases C-2 and D-2 are approximately 25% greater at 0.35 chord and 71% less at the trailing edge compared to C-1 and D-1.

Figure 15d illustrates the heat absorbed by each layer of the panel over 900 s of flight. All four cases are in close agreement for each layer, which indicates that the average layer temperature is approximately the same for each case. Since the radiation shield is the first layer exposed to aerodynamic heating, it has the steepest initial increase in heat absorbed. Consistent with this effect, the thermal insulation has the second steepest initial increase. Both the radiation shield and the thermal insulation reach approximately constant values of heat absorbed within 120 s. However, the plate structure continues to absorb heat at approximately a constant rate from 120 to 900 s.

Stress in the plate structure that results from the combined effects of in-plane stretching, transverse bending, and temperature distribution, is shown in Figs. 16a and 16b at the initial time, 300 s, and 900 s. Stress at the upper surface is illustrated in Fig. 16a and at the lower surface in Fig. 16b. Note that the upper and lower surface stresses are approximately equal in magnitude and opposite in sign at each location along the plate, indicating that the bending stress is dominant. The stress distributions are similar for each case (C-1, C-2, D-1, and D-2). This is expected based on the dominance of the
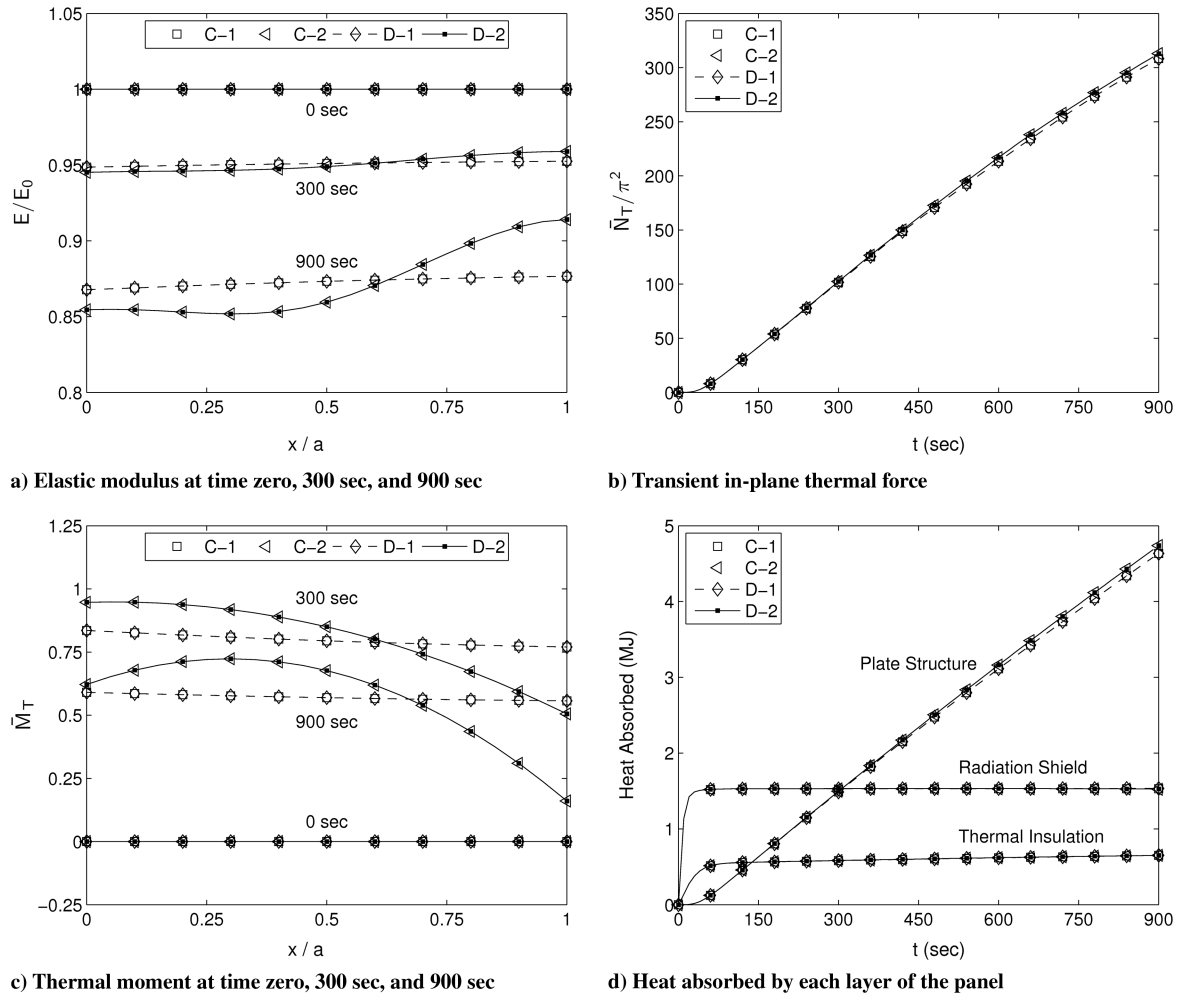
a) Elastic modulus at time zero, 300 sec, and 900 sec

b) Transient in-plane thermal force

c) Thermal moment at time zero, 300 sec, and 900 sec

d) Heat absorbed by each layer of the panel

Fig. 15 Material property degradation and thermal loading during dynamically stable aerothermoelastic response at $M_\infty = 8.0$.
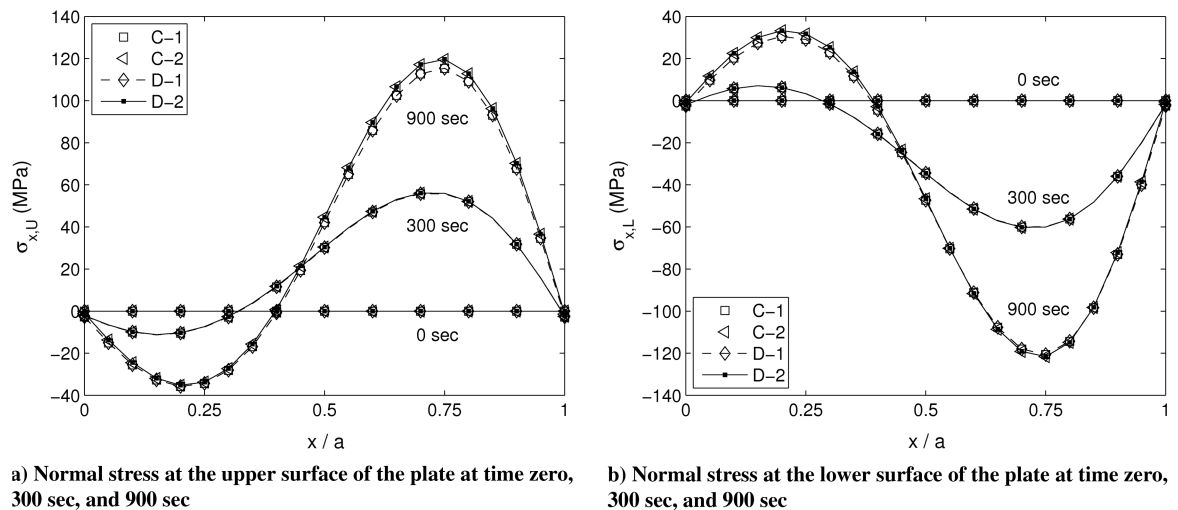

a) Normal stress at the upper surface of the plate at time zero, 300 sec, and 900 sec

b) Normal stress at the lower surface of the plate at time zero, 300 sec, and 900 sec

Fig. 16 Stress in the plate structure during dynamically stable aerothermoelastic response at $M_\infty = 8.0$.

bending stress and the close agreement of the deformed panel shapes illustrated in Fig. 14a. The largest difference occurs at 900 s, where the magnitude of the peak stresses from cases C-2 and D-2 (two-way coupling) are 3.7% greater at the upper surface compared to C-1 and D-1 (one-way coupling).

V.   Conclusions

A comprehensive aerothermoelastic model is developed for analysis of panel structures in hypersonic flow. Multiple, systematic studies are performed to investigate the impact of fluid–thermal–structural coupling on aerothermoelastic behavior: i.e., on flutter boundary predictions, nonlinear flutter response, and dynamically stable response. Multiple important effects are included in the analysis: namely, 1) mutual coupling between elastic deformation and aerodynamic heating (i.e., two-way coupling), 2) transient arbitrary in-plane and through-thickness temperature distributions, and 3) the associated thermal stresses and material property degradations. In addition, two simplified approaches are investigated for reducing the computational expense of comprehensive aerothermoelastic analysis

in hypersonic flow, these are 1) quasi-static coupling and 2) time-averaged dynamic coupling of aerothermal and aeroelastic solutions. The results of these studies allow one to reach several useful conclusions:

1) Thermal stresses result in significant reductions to the unheated panel flutter boundary. Material property degradation at elevated temperatures, in addition to thermal stresses, further reduces this boundary. For the panel investigated, one-way and two-way coupled solutions that include these effects show general agreement of the flutter boundary predictions. However, a small difference (less than 10%) between one-way and two-way coupling is evident at the lower Mach numbers considered: i.e., when longer-duration exposure to aerodynamic heating is required to degrade the material properties to the point of flutter. In such cases, one-way coupling gives a nonconservative prediction of the flutter boundary compared to two-way coupling.

2) Quasi-static coupling, time-averaged dynamic coupling, and instantaneous dynamic coupling approaches yield nearly identical flutter boundary predictions. Thus, quasi-static or time-averaged dynamic coupling procedures may be used to reduce computational cost with little loss in accuracy of flutter prediction.

3) There is no additional computational expense associated with two-way coupling for the comprehensive aerothermoelastic model developed in this work, whether quasi-static or dynamic coupling is used.

4) Before flutter (i.e., for dynamically stable response), quasi-static coupling and dynamic coupling yield nearly identical results. Two-way coupling results in nonuniform aerodynamic heating compared to one-way coupling, which produces: nonuniform temperature distributions along the surface and throughout the panel, nonuniform material property degradations, and nonuniform thermal bending moments. These nonuniformities result in localized regions in which material temperature limits may be exceeded, and they impact flutter boundary predictions and nonlinear flutter response.

5) After the onset of flutter (i.e., for nonlinear flutter response), the response is sensitive to the use of time-averaged versus instantaneous dynamic coupling, as well as to one-way versus two-way coupling. However, since time-averaged coupling and one-way coupling produce accurate results for some dynamic responses, additional work is needed to fully characterize their use.

Acknowledgments

References

[1] Mansour, N., Pittman, J., and Olson, L., "Fundamental Aeronautics Hypersonics Project: Overview," AIAA Paper 2007-4263, June 2007.
[2] Walker, S. H., and Rodgers, F., "Falcon Hypersonic Technology Overview," AIAA Paper 2005-3253, May 2005.
[3] Kazmar, R., "Airbreathing Hypersonic Propulsion at Pratt and Whitney—Overview," AIAA Paper 2005-3256, May 2005.
[4] Dolvin, D. J., "Hypersonic International Flight Research and Experimentation (HIFiRE) Fundamental Sciences and Technology Development Strategy," AIAA Paper 2008-2581, April–May 2008.
[5] Bolender, M. A., and Doman, D. B., "Nonlinear Longitudinal Dynamic Model of an Air-Breathing Hypersonic Vehicle," *Journal of Spacecraft and Rockets*, Vol. 44, No. 2, March–April 2007, pp. 374–387.
doi:10.2514/1.23370
[6] Spottswood, S. M., Hollkamp, J. J., and Eason, T. G., "On the use of Reduced-Order Models for a Shallow Curved Beam under Combined Loading," AIAA Paper 2008-2235, April 2008.
[7] Cazier, F. W., Jr., and Ricketts, R. H., "Structural Dynamic and Aeroelastic Considerations for Hypersonic Vehicles," AIAA Paper 1991-1255, April 1991.

[8] Ricketts, R. H., Noll, T. E., Whitlow, W., Jr., and Huttsell, L. J., "An Overview of Aeroelasticity Studies for the National Aero-Space Plane," AIAA Paper 1993-1313, April 1993.
[9] Gupta, K. K., Voelker, L. S., Bach, C., Doyle, T., and Hahn, E., "CFD-Based Aeroelastic Analysis of the X-43 Hypersonic Flight Vehicle," AIAA Paper 2001-712, Jan. 2001.
[10] Berry, S. A., Horvath, T. J., Hollis, B. R., Thompson, R. A., and Hamilton, H. H., "X-33 Hypersonic Boundary Layer Transition," AIAA Paper 1999-3560, June–July 1999.
[11] Riley, C. J., Kleb, W. L., and Alter, S. J., "Aeroheating Predictions for X-34 Using an Inviscid-Boundary Layer Method," AIAA Paper 1999-880, Jan. 1999.
[12] Bertin, J. J., *Hypersonic Aerothermodynamics*, AIAA, Reston, VA, 1994.
[13] Anderson, J. D., Jr., *Hypersonic and High-Temperature Gas Dynamics*, 2nd ed., AIAA, Reston, VA, 2006.
[14] Blankson, I. M., "Air-Breathing Hypersonic Waveriders: A Survey of Research Needs," *Proceedings of the First International Waverider Symposium*, Univ. of Maryland, College Park, MD, Oct. 1990.
[15] Bertin, J. J., and Cummings, R. M., "Fifty Years of Hypersonics: Where We've Been and Where We're Going," *Progress in Aerospace Sciences*, Vol. 39, April 2003, pp. 511–536.
doi:10.1016/S0376-0421(03)00079-4
[16] Fidan, B., Mirmirani, M., and Ionnou, P., "Flight Dynamics and Control of Air-Breathing Hypersonic Vehicles: Review and New Directions," AIAA Paper 2003-7081, Dec. 2003.
[17] Dugundji, J., and Calligeros, J. M., "Similarity Laws for Aerothermoelastic Testing," *Journal of the Aero/Space Sciences*, Vol. 29, No. 8, Aug. 1962, pp. 935–950.
[18] McNamara, J. J., and Friedmann, P. P., "Aeroelastic and Aerothermoelastic Analysis of Hypersonic Vehicles: Current Status and Future Trends," AIAA Paper 2007-2013, April 2007.
[19] Bisplinghoff, R. L., "Some Structural and Aeroelastic Considerations of High-Speed Flight," *Journal of the Aeronautical Sciences*, Vol. 23, No. 4, April 1956, pp. 289–329,367.
[20] Budiansky, B., and Mayers, J., "Influence of Aerodynamic Heating on the Effective Torsional Stiffness of Thin Wings," *Journal of the Aeronautical Sciences*, Vol. 23, No. 12, Dec. 1956, pp. 1081–1093,1108.
[21] Biot, M. A., "Influence of Thermal Stresses on the Aeroelastic Stability of Supersonic Wings," *Journal of the Aeronautical Sciences*, Vol. 24, No. 6, June 1957, pp. 418–420,429.
[22] Runyan, H. L., and Jones, N. H., "Effect of Aerodynamic Heating on the Flutter of a Rectangular Wing at a Mach Number of 2," NACA RM L58C31, 1958.
[23] Rogers, M., "Aerothermoelasticity," *Aero/Space Engineering*, Vol. 17, No. 10, Oct. 1958, pp. 34–43,64.
[24] Bisplinghoff, R. L., and Dugundji, J., *Influence of Aerodynamic Heating on Aeroelastic Phenomena*, Pergamon, New York, 1958, pp. 288–312.
[25] Houbolt, J. C., "A Study of Several Aerothermoelastic Problems of Aircraft Structures in High-Speed Flight," Ph.D. Thesis, Swiss Federal Inst. of Technology, Zurich, 1958.
[26] Garrick, I. E., "A Survey of Aerothermoelasticity," *Aero/Space Engineering*, Vol. 22, No. 1, Jan. 1963, pp. 140–147.
[27] Hedgepeth, J., and Widmayer, E., Jr., "Dynamic and Aeroelastic Problems of Lifting Re-Entry Bodies," *Aero/Space Engineering*, Vol. 22, No. 1, Jan. 1963, pp. 148–153.
[28] Laidlaw, W. R., and Wykes, J. H., "Potential Aerothermoelastic Problems Associated with Advanced Vehicle Design," *Aero/Space Engineering*, Vol. 22, No. 1, Jan. 1963, pp. 154–164.
[29] Mei, C., Abdel-Motagaly, K., and Chen, R., "Review of Nonlinear Panel Flutter at Supersonic and Hypersonic Speeds," *Applied Mechanics Reviews*, Vol. 52, No. 10, Oct. 1999, pp. 321–332.
doi:10.1115/1.3098919
[30] Abbas, J. F., Ibrahim, R. A., and Gibson, R. F., "Nonlinear Flutter of Orthotropic Composite Panel Under Aerodynamic Heating," *AIAA Journal*, Vol. 31, No. 8, Aug. 1993, pp. 1478–1488.
doi:10.2514/3.11798
[31] Gee, D. J., and Sipcic, S. R., "Coupled Thermal Model for Nonlinear Panel Flutter," *AIAA Journal*, Vol. 37, No. 5, May 1999, pp. 642–650.
doi:10.2514/2.765
[32] Pourtakdoust, S. H., and Fazelzadeh, S. A., "Nonlinear Aerothermoelastic Behavior of Skin Panel with Wall Shear Stress Effect," *Journal of Thermal Stresses*, Vol. 28, No. 2, Feb. 2005, pp. 147–169.
doi:10.1080/014957390523714
[33] Fung, Y. C., "On Two-Dimensional Panel Flutter," *Journal of the Aeronautical Sciences*, Vol. 25, No. 4, March 1958, pp. 145–160.

[34] Ventres, C. S., and Dowell, E. H., "Comparison of Theory and Experiment for Nonlinear Flutter of Loaded Plates," *AIAA Journal*, Vol. 8, No. 11, Nov. 1970, pp. 2022–2030.
doi:10.2514/3.6041

[35] Yang, T. Y., and Han, A. D., "Flutter of Thermally Buckled Finite Element Panels," *AIAA Journal*, Vol. 14, No. 7, July 1976, pp. 975–977.
doi:10.2514/3.7173

[36] Dixon, I. R., and Mei, C., "Nonlinear Flutter of Rectangular Composite Panels Under Uniform Temperature Using Finite Elements," *Nonlinear Vibrations*, Winter Annual Meeting, American Society of Mechanical Engineers, New York, 1992, pp. 123–132.

[37] Bein, T., Friedmann, P., Zhong, X., and Nydick, I., "Hypersonic Flutter of a Curved Shallow Panel with Aerodynamic Heating," AIAA Paper 1993-1318, April 1993.

[38] Zhou, R. C., Xue, D. Y., and Mei, C., "Finite Element Time Domain—Modal Formulation for Nonlinear Flutter of Composite Panels," *AIAA Journal*, Vol. 32, No. 10, Oct. 1994, pp. 2044–2052.
doi:10.2514/3.12250

[39] Udrescu, R., and Surace, G., "Enhanced Aeroelastic Analysis of Panels Under Transitory Hypersonic Flow Conditions," *AIAA Journal*, Vol. 38, No. 5, May 2000, pp. 755–761.
doi:10.2514/2.1046

[40] Oh, I. K., Lee, I., and Lee, D. M., "Non-Linear Transient Response of Fluttering Stiffened Composite Plates Subject to Thermal Load," *Journal of Sound and Vibration*, Vol. 245, No. 4, 2001, pp. 715–736.
doi:10.1006/jsvi.2001.3576

[41] Lee, I., Roh, J.-H., and Oh, I.-K., "Aerothermoelastic Phenomena of Aerospace and Composite Structures," *Journal of Thermal Stresses*, Vol. 26, 2003, pp. 525–546.
doi:10.1080/713855957

[42] Ibrahim, H. H., Tawfik, M., and Al-Ajmi, M., "Thermal Buckling and Nonlinear Flutter Behavior of Functionally Graded Material Panels," *Journal of Aircraft*, Vol. 44, No. 5, Sept.–Oct. 2007, pp. 1610–1618.
doi:10.2514/1.27866

[43] Schaeffer, H. G., and Heard, W. L., Jr., "Flutter of a Flat Panel Subjected to a Nonlinear Temperature Distribution," *AIAA Journal*, Vol. 3, No. 10, Oct. 1965, pp. 1918–1923.
doi:10.2514/3.3280

[44] Xue, D. Y., and Mei, C., "Finite Element Nonlinear Flutter and Fatigue Life of Two-Dimensional Panels with Temperature Effects," *Journal of Aircraft*, Vol. 30, No. 6, Nov.–Dec. 1993, pp. 993–999.
doi:10.2514/3.46444

[45] Liaw, D. G., "Nonlinear Supersonic Flutter of Laminated Composite Plates Under Thermal Loads," *Computers and Structures*, Vol. 65, No. 5, 1997, pp. 733–740.
doi:10.1016/S0045-7949(94)00487-0

[46] Librescu, L., Marzocca, P., and Silva, W. A., "Linear/Nonlinear Supersonic Panel Flutter in a High-Temperature Field," *Journal of Aircraft*, Vol. 41, No. 4, July–Aug. 2004, pp. 918–924.
doi:10.2514/1.679

[47] Xue, D. Y., and Mei, C., "Finite Element Nonlinear Panel Flutter with Arbitrary Temperatures in Supersonic Flow," *AIAA Journal*, Vol. 31, No. 1, Jan. 1993, pp. 154–162.
doi:10.2514/3.11332

[48] Nydick, I., Friedmann, P. P., and Zhong, X., "Hypersonic Panel Flutter Studies on Curved Panels," AIAA Paper 1995-1485, April 1995.

[49] Cheng, G., Lee, Y. Y., and Mei, C., "Flow Angle, Temperature, and Aerodynamic Damping on Supersonic Panel Flutter Stability Boundary," *Journal of Aircraft*, Vol. 40, No. 2, March–April 2003, pp. 248–255.
doi:10.2514/2.3116

[50] Cheng, G., and Mei, C., "Finite Element Modal Formulation for Hypersonic Panel Flutter Analysis with Thermal Effects," *AIAA Journal*, Vol. 42, No. 4, April 2004, pp. 687–695.
doi:10.2514/1.9553

[51] Prakash, T., and Ganapathi, M., "Supersonic Flutter Characteristics of Functionally Graded Flat Panels Including Thermal Effects," *Composite Structures*, Vol. 72, 2006, pp. 10–18.
doi:10.1016/j.compstruct.2004.10.007

[52] Ghoman, S., Mei, C., and Azzouz, M. S., "Frequency Domain Method for Flutter Analysis of Curved Panels under Yawed Supersonic Flow at Elevated Temperature," AIAA Paper 2008-2312, April 2008.

[53] Ashley, H., and Zartarian, G., "Piston Theory—A New Aerodynamic Tool for the Aeroelastician," *Journal of the Aeronautical Sciences*, Vol. 23, No. 12, Dec. 1956, pp. 1109–1118.

[54] Thornton, E. A., and Dechaumphai, P., "Coupled Flow, Thermal, and Structural Analysis of Aerodynamically Heated Panels," *Journal of Aircraft*, Vol. 25, No. 11, Nov. 1988, pp. 1052–1059.
doi:10.2514/3.45702

[55] Dechaumphai, P., Thornton, E. A., and Wieting, A. R., "Flow-Thermal-Structural Study of Aerodynamically Heated Leading Edges," *Journal of Spacecraft and Rockets*, Vol. 26, No. 4, July–Aug. 1989, pp. 201–209.
doi:10.2514/3.26055

[56] Kontinos, D., "Coupled Thermal Analysis Method with Application to Metallic Thermal Protection Panels," *Journal of Thermophysics and Heat Transfer*, Vol. 11, No. 2, April–June 1997, pp. 173–181.
doi:10.2514/2.6249

[57] Rodgers, J. P., "Aerothermoelastic Analysis of a NASP-Like Vertical Fin," AIAA Paper 1992-2400, April 1992.

[58] Heeg, J., Zeiler, T. A., Pototzky, A. S., Spain, C. V., and Engelund, W. C., "Aerothermoelastic Analysis of a NASP Demonstrator Model," AIAA Paper 1993-1366, April 1993.

[59] Heeg, J., Gilbert, M. G., and Pototzky, A. S., "Active Control of Aerothermoelastic Effects for a Conceptual Hypersonic Aircraft," *Journal of Aircraft*, Vol. 30, No. 4, July–Aug. 1993, pp. 453–458.
doi:10.2514/3.56890

[60] McNamara, J. J., Friedmann, P. P., Powell, K. G., Thuruthimattam, B. J., and Bartels, R. E., "Aeroelastic and Aerothermoelastic Behavior in Hypersonic Flow," *AIAA Journal*, Vol. 46, No. 10, Oct. 2008, pp. 2591–2610.
doi:10.2514/1.36711

[61] Anderson, J. D., Jr., *Modern Compressible Flow with Historical Perspective*, 3rd ed., McGraw–Hill, New York, 2003.

[62] Bailie, J. A., and McFeely, J. E., "Panel Flutter in Hypersonic Flow," *AIAA Journal*, Vol. 6, No. 2, Feb. 1968, pp. 332–337.
doi:10.2514/3.4498

[63] McNamara, J. J., Gogulapati, A., Friedmann, P. P., and Banavara, N. K., "Approximate Modeling of Unsteady Aerodynamic Loads in Hypersonic Aeroelasticity," International Forum on Aeroelasticity and Structural Dynamics, Paper 2007-099, Stockholm, Sweden, June 2007.

[64] Eckert, E. R. G., "Engineering Relations for Heat Transfer and Friction in High-Velocity Laminar and Turbulent Boundary-Layer Flow Over Surfaces With Constant Pressure and Temperature," *Transactions of the ASME*, Vol. 78, No. 6, Aug. 1956, pp. 1273–1283.

[65] Zoby, E. V., Moss, J. N., and Sutton, K., "Approximate Convective-Heating Equations for Hypersonic Flows," *Journal of Spacecraft and Rockets*, Vol. 18, No. 1, Jan.–Feb. 1981, pp. 64–70.
doi:10.2514/3.57788

[66] DeJarnette, F. R., Hamilton, H. H., Weilmuenster, K. J., and Cheatwood, F. M., "A Review of Some Approximate Methods Used in Aerodynamic Heating Analyses," *Journal of Thermophysics and Heat Transfer*, Vol. 1, No. 1, Jan. 1987, pp. 5–12.
doi:10.2514/3.1

[67] Tauber, M. E., "A Review of High-Speed, Convective, Heat-Transfer Computation Methods," NASA TP-2914, 1989.

[68] Riley, C. J., and DeJarnette, F. R., "Engineering Aerodynamic Heating Method for Hypersonic Flow," *Journal of Spacecraft and Rockets*, Vol. 29, No. 3, May–June 1992, pp. 327–334.
doi:10.2514/3.26355

[69] Hamilton, H. H., Greene, F. A., and DeJarnette, F. R., "Approximate Method for Calculating Heating Rates on Three-Dimensional Vehicles," *Journal of Spacecraft and Rockets*, Vol. 31, No. 3, May–June 1994, pp. 345–354.
doi:10.2514/3.26446

[70] Kinney, D. J., Garcia, J. A., and Huynh, L., "Predicted Convective and Radiative Aerothermodynamic Environments for Various Reentry Vehicles Using CBAERO," AIAA Paper 2006-659, Jan. 2006.

[71] Zoby, E. V., and Graves, R. A., Jr., "Comparison of Turbulent Prediction Methods with Ground and Flight Test Heating Data," *AIAA Journal*, Vol. 15, No. 7, July 1977, pp. 901–902.
doi:10.2514/3.60729

[72] Hilsenrath, J., Hoge, H. J., Beckett, C. W., Masi, J. F., Benedict, W. S., Nuttall, R. L., et al., *Tables of Thermodynamic and Transport Properties of Air, Argon, Carbon Dioxide, Carbon Monoxide, Hydrogen, Nitrogen, Oxygen, and Steam*, Pergamon, New York, 1960.

[73] Myers, D. E., Martin, C. J., and Blosser, M. L., "Parametric Weight Comparison of Advanced Metallic, Ceramic Tile, and Ceramic Blanket Thermal Protection Systems," NASA TM 2000-210289, June 2000.

[74] Shih, P. K., Prunty, J., and Mueller, R. N., "Thermostructural Concepts for Hypervelocity Vehicles," *Journal of Aircraft*, Vol. 28, No. 5, May–June 1991, pp. 337–345.
doi:10.2514/3.46032

[75] "Metallic Materials and Elements for Aerospace Vehicle Structures," U.S. Department of Defense, MIL-HDBK-5J, Jan. 2003.

[76] Tannehill, J. C., Anderson, D. A., and Pletcher, R. H., *Computational Fluid Mechanics and Heat Transfer*, 2nd ed., Taylor and Francis, Philadelphia, 1997.

[77] Holman, J. P., *Heat Transfer*, 8th ed., McGraw–Hill, New York, 1997.

[78] Bolotin, V. V., *Nonconservative Problems of the Theory of Elastic Stability*, Pergamon, New York, 1963, pp. 274–312.

[79] Dowell, E. H., "Nonlinear Oscillations of a Fluttering Plate," *AIAA Journal*, Vol. 4, No. 7, July 1966, pp. 1267–1275.
doi:10.2514/3.3658

[80] Thornton, E. A., *Thermal Structures for Aerospace Applications*, AIAA, Reston, VA, 1996, pp. 253–284.

[81] Felippa, C. A., Park, K. C., and Farhat, C., "Partitioned Analysis of Coupled Mechanical Systems," *Computer Methods in Applied Mechanics and Engineering*, Vol. 190, 2001, pp. 3247–3270.
doi:10.1016/S0045-7825(00)00391-1

[82] Hodges, D. H., and Pierce, G. A., *Introduction to Structural Dynamics and Aeroelasticity*, Cambridge Univ. Press, New York, 2002.

[83] Chapra, S. C., and Canale, R. P., *Numerical Methods for Engineers: With Programming and Software Applications*, 3rd ed., McGraw–Hill, New York, 1998.

[84] Glass, C. E., and Hunt, L. R., "Aerothermal Tests of Spherical Dome Protuberances on a Flat Plate at a Mach Number of 6.5," NASA TP-2631, 1986.

[85] Deveikis, W. D., and Hunt, L. R., "Loading and Heating of a Large Flat Plate at Mach 7 in the Langley 8-Foot High-Temperature Structures Tunnel," NASA TN D-7275, Sept. 1973.

[86] Deveikis, W. D., Bruce, W. E., Jr., and Karns, J. R., "Techniques for Aerothermal Tests of Large, Flightweight Thermal Protection Panels in a Mach 7 Wind Tunnel," NASA TM X-71983, July 1974.

[87] Leyhe, E. W., and Howell, R. R., "Calculation Procedure for Thermodynamic, Transport, and Flow Properties of the Combustion Products of a Hydrocarbon Fuel Mixture Burned in Air with Results for Ethylene-Air and Methane-Air Mixtures," NASA TN D-914, Jan. 1962; also Errata, May 1965.

[88] Crowell, A. R., Culler, A. J., and McNamara, J. J., "Reduced Order Aerothermodynamics for Two-Way Coupled Aerothermoelasticity in Hypersonic Flow," International Forum on Aeroelasticity and Structural Dynamics, Paper 2009-094, Seattle, WA, June 2009.

[89] *MATLAB Product Help Manual*, Ver. 7.6 (R2008a), The MathWorks, Inc., Natick, MA, 2008.

[90] Tseng, W.-Y., and Dugundji, J., "Nonlinear Vibrations of a Buckled Beam Under Harmonic Excitation," *Journal of Applied Mechanics*, Vol. 38, No. 2, June 1971, pp. 467–476.

E. Livne
Associate Editor